Defence Research and Development Canada
Recherche et développement pour la défense Canada

DRDC | RDDC

A virtual instrument for Micro-Doppler analysis of signals in SAR/ISAR: Parameters estimation and focusing moving targets

T. Thayaparan
DRDC - Ottawa Research Centre

Defence Research and Development Canada

Scientific Report
DRDC-RDDC-2014-R6
December 2014

Canada

A virtual instrument for Micro-Doppler analysis of signals in SAR/ISAR: Parameters estimation and focusing moving targets

T. Thayaparan
DRDC - Ottawa Research Centre

Defence Research and Development Canada

Scientific Report

DRDC-RDDC-2014-R6

December 2014

© Her Majesty the Queen in Right of Canada, as represented by the Minister of National Defence, 2014
© Sa Majesté la Reine (en droit du Canada), telle que représentée par le minister de la Défense nationale, 2014

Abstract

The micro-Doppler (m-D) effect appears in the synthetic aperture radar (SAR)/inverse SAR (ISAR) image of a target whenever the target has one or more rotating or vibrating parts. M-D effect introduces distortion in the SAR/ISAR images. On the other hand, m-D effect also carries information about the features of moving parts of a stationary or moving target that can be used for target identification purpose. Based on L-statistics, spectrogram, and inverse Radon transform, a radar data exploitation Matlab toolbox was develped for classifying air, land and ocean targets, which helps Geospatial Intelligence (GEOINT) support to Canadian Forces. This toolbox will scan and search any M-D activity in the desired area of the SAR/ISAR image. The toolbox has three options; 1) Focus the stationary target if there is no m-D, 2) Focus the target after removing the m-D, and 3) extract the m-D and determine the motion parameters. The toolbox was tested and validated against a variety of simulated and measured targets.

Significance for defence and security

The micro-Doppler (m-D) effect appears in the synthetic aperture radar (SAR) image of a target whenever the target has one or more rotating or vibrating parts. Similar effect appears in the inverse synthetic aperture radar (ISAR) imaging, as well. If the frequency modulations on the returned signal caused by the moving parts are not filtered, then the m-D effect can introduce distortion in the SAR/ISAR images. The frequency content of the m-D signal changes over time in a wide range. Therefore, the m-D may cover the rigid body and make it difficult to detect. On the other hand, the m-D effect also carries useful information about the features of moving parts of a target (type, velocity, size, etc.) that are complementary to existing target recognition methods. It is easier to estimate these features if the m-D effect is separated from the rigid body part of the radar image. Thus, the extraction of m-D effects from the radar images have attracted significant research attention, especially the image enhancement and m-D extraction for the spacebourse sensors such as RADARSAT-2 and TerraSAR-X.

Based on L-statistics, spectrogram, and inverse Radon transform, a radar data exploitation Matlab toolbox was develped for classifying air and land targets. This toolbox will scan and search any m-D activity in the desired area of the SAR/ISAR image. The toolbox has three options; 1) Focus the stationary target if there is no m-D, 2) Focus the target after removing the m-D, and 3) extract the m-D and determine the motion parameters such as rotation/vibration rate, initial phase, and amplitude of the stationary and moving targets. The toolbox was tested and validated against a variety of simulated and measured targets.

The m-D toolbox can be used to identify important classes of battlefield targets. The m-D signatures of vibrating and rotating structures can be used to differentiate and identify specific types of military vehicles/tanks/trucks and determine their movement and the speed of their engines. This approach could provide improved target signature/feature recognition over current audio classification techniques. In addition to battlefield land targets, important classes of air and ocean targets can also be distinguished by their m-D signatures, for example, radar signals returned from military targets that incorporate vibrating or rotating structures such as aircraft propellers, helicopter rotors, rotating antennas on a ship or an aircraft contains m-D signatures related to these structures. One of the important applications of the m-D is the detection of a hovering helicopter by hub radar returns through m-D features rather than the blade flash returns, which is currently used by conventional scanning radars. Radar returns from the engine compressor and blade assemblies of a jet aircraft contain jet engine modulation that also generates m-D. Hence the m-D toolbox offers a new way for the analysis of military target signatures. It provides additional and unique target features that are complementary to those made available by existing methods. The toolbox will be available to the CFJIC (Canadian Forces Joint Imagery Centre) and MCE (Mapping and Charting Establishment) clients for Geospatial Intelligence (GEOINT) support.

Radar gait image analysis integrated with m-D can provide new identification methods for remote detection of walking personnel either in battlefield or urban scenarios. This technique can be applied to other areas as well: countering terrorism, conducting urban military operations, providing urban border security, dealing with hostage acts, intercepting suicide bombers, and detecting humans (soldiers) in a forest. Distance is the key factor, because terrorists and other criminals often act from afar, and the earlier detection means a quicker response. Therefore, as a new identification/recognition tool for operational radar Automatic Gait Recognition (AGR) system, m-D has the good potential for significantly improving military capabilities and protection for CF and CF facilities.

Résumé

L'effet micro-Doppler (m-D) apparaît dans l'image d'un radar à synthèse d'ouverture (SAR) ou d'un radar à synthèse d'ouverture inverse (ISAR) d'une cible qui comporte au moins une pièce tournante ou vibrante. L'effet m-D introduit de la distorsion dans les images SAR ou ISAR. Par contre, cet effet fournit aussi des renseignements sur les caractéristiques des pièces mobiles d'une cible fixe ou en mouvement, renseignements qui peuvent servir à identifier la cible. À partir des statistiques linéaires, du spectrogramme et de la transformée inverse de Radon, une boîte à outils Matlab d'exploitation des données radar a été mise au point pour classer les cibles aériennes, terrestres et océaniques afin d'aider au soutien du renseignement géospatial (GEOINT) des Forces canadiennes. Cette boîte à outils balaie la zone désirée de l'image SAR ou ISAR à la recherche d'activités m-D. Elle comporte trois options : 1) la focalisation de la cible fixe en l'absence de m-D; 2) la focalisation de la cible après l'élimination des m-D; 3) l'extraction des m-D et la détermination des paramètres de mouvement. Elle a en outre été mise à l'essai et validée en fonction de diverses cibles simulées et mesurées.

Importance pour la défense et la sécurité

L'effet micro-Doppler (m-D) apparaît dans l'image d'un radar à synthèse d'ouverture (SAR) d'une cible qui comporte au moins une pièce tournante ou vibrante. Un effet similaire apparaît aussi dans l'image d'un radar à synthèse d'ouverture inverse (ISAR). Si les modulations de fréquence sur les signaux réfléchis causés par les pièces mobiles ne sont pas filtrées, l'effet m-D peut introduire des distorsions dans les images SAR ou ISAR. De plus, le contenu fréquentiel du signal m-D varie en fonction du temps sur une large gamme de fréquences. En conséquence, l'effet m-D peut couvrir un corps rigide et le rendre difficile à détecter. Par contre, il contient aussi des renseignements utiles sur les caractéristiques des pièces mobiles d'une cible (type, vitesse, dimensions, etc.), renseignements qui sont complémentaires aux méthodes existantes de reconnaissance de cibles. Ces caractéristiques sont plus faciles à évaluer si l'effet m-D est séparé de la partie rigide de la cible dans l'image radar. L'extraction des effets m-D des images radar fait donc l'objet de beaucoup de recherches, surtout relativement à l'amélioration des images et à l'extraction des m-D pour les capteurs spatiaux comme RADARSAT-2 et TerraSAR-X.

À partir des statistiques linéaires, du spectrogramme et de la transformée inverse de Radon, une boîte à outils Matlab d'exploitation des données radar a été mise au point pour classer les cibles aériennes et terrestres. Cette boîte à outils balaie la zone désirée de l'image SAR ou ISAR à la recherche d'activités m-D. Elle comporte trois options : 1) la focalisation de la cible fixe en l'absence de m-D; 2) la focalisation de la cible après le retrait des m-D; 3) l'extraction des m-D et la détermination des paramètres de mouvement

comme la vitesse de rotation et de vibration, la phase initiale et l'amplitude des cibles fixes et mobiles. Elle a en outre été mise à l'essai et validée en fonction de diverses cibles simulées et mesurées. La boîte à outils m-D peut être utilisée pour identifier des classes importantes de cibles sur le champ de bataille. Les signatures m-D de structures vibrantes et tournantes peuvent servir à différencier et à identifier des types particuliers de véhicules, de chars et de camions militaires,

ainsi qu'à déterminer leur mouvement et la vitesse de leurs moteurs. Par rapport aux techniques actuelles de classification audio, cette méthode pourrait améliorer la reconnaissance de la signature et des caractéristiques d'une cible. En plus des cibles terrestres sur les champs de bataille, des classes importantes de cibles aériennes et océaniques peuvent aussi être distinguées au moyen de leurs signatures m-D. Les signaux radar renvoyés par des cibles militaires dotées de structures vibrantes et tournantes, comme les hélices d'aéronef, les rotors d'hélicoptère et les antennes rotatives d'un navire ou d'un aéronef, comportent des signatures m-D associées à ces structures. Une application importante de l'effet m-D est la détection d'un hélicoptère en vol stationnaire par les échos radar du moyeu de rotor au moyen de leurs caractéristiques m-D plutôt que par les éclairs de pales qu'utilisent aujourd'hui les radars à balayage traditionnels. Les échos radar provenant des aubes et du compresseur de moteur d'un avion à réaction contiennent une modulation qui produit aussi des effets m-D. Par conséquent, la boîte à outils pour m-D offre une nouvelle méthode d'analyse des signatures de cibles militaires. Elle fournit en outre des caractéristiques de cibles supplémentaires et uniques qui sont complémentaires à celles produites par les méthodes actuelles. Elle sera offerte aux clients du Centre d'imagerie interarmées des Forces canadiennes (CIIFC) et du Service de cartographie (S Carto) aux fins de soutien du renseignement géospatial (GEOINT).

L'intégration de l'analyse de la démarche dans les images radar et de l'effet m-D fournit de nouvelles méthodes d'identification pour la détection à distance de marcheurs dans des scénarios de bataille ou des scénarios urbains. Cette technique peut aussi s'appliquer à d'autres domaines : lutte contre le terrorisme, conduite d'opérations militaires en zone urbaine, prestation de services de sécurité à la frontière en zone urbaine, interventions dans les situations de prise d'otages, interception de bombes humaines et détection d'êtres humains (soldats) en forêt. La distance constitue un facteur clé, car les terroristes et les autres criminels agissent souvent de loin, et une détection plus précoce permet une réponse plus rapide. Par conséquent, en tant que nouvel outil d'identification et de reconnaissance pour le système opérationnel de reconnaissance automatique de la démarche (AGR), l'effet m-D peut améliorer de façon considérable les capacités militaires et la protection pour les Forces canadiennes et leurs installations.

Table of contents

Abstract i

Significance for defence and security i

Résumé iii

Importance pour la défense et la sécurité iii

Table of contents v

List of figures vii

1 Introduction 1

2 Estimation of micro-Doppler motion parameters 2

2.1 Radon and inverse Radon transform 3

2.2 Parameters estimation 4

2.3 Method implementation 6

2.4 Multicomponent signal analysis 9

2.5 Nonsinusoidally modulated signals 12

2.6 Analysis using partial data 13

2.7 Experimental data: rotating antenna in SAR 15

2.8 Experimental data: hovering helicopter 15

3 Micro-Doppler removal in the radar imaging analysis 19

3.1 Time-frequency analysis and L-statistics 20

3.1.1 Restoring the high FT concentration from the STFT 20

3.1.2 Basic idea for the separation of a rigid body and fast rotating part 22

3.1.3 Adaptive percentage of missing values 27

3.1.4 Algorithm for the micro-Doppler effects removal 29

3.2 Results 31

4 Micro-Doppler toolbox 43
4.1 Files and installation 44
4.2 Virtual instrument 44
4.2.1 Main screen 44
4.2.2 Time-frequency data representation 48
4.2.3 L-statistics 48
4.2.4 Micro-Doppler parameter estimation 49
4.2.5 2D data analysis 53
4.2.6 Demo 53
4.3 Time-Frequency Toolbox 53
4.3.1 Files and installation 55
4.3.2 Demo 55
4.3.3 Advanced visualization 55
5 Conclusion 60
References 61

List of figures

Figure 1: Modulation parameters estimation for the mono-component non-noisy sinusoidally FM signal. Time frequency representation (a), (b); concentration measure (c), (d); inverse Radon transform with highest concentration (e), (f) and inverse Radon transform when the parameter α is not optimally chosen (g), (h). 8

Figure 2: Parameter estimation of the noisy signal with SNR $= 0\,\mathrm{dB}$ (a), (b) and the multicomponent signal (c), (d). Estimated modulation is plotted with black line over the spectrogram image. 9

Figure 3: Multicomponent signal. Estimation of the first component (a), (b); the second component (c), (d); and the third component (e) and (f). Each component is removed from the signal after the estimation, according to the described procedure, prior to next component estimation. 11

Figure 4: Nonsinusoidal modulation. Triangulary modulated signal (a), (b); Signal with nonsinusoidal modulation and varying amplitude (c), (d). 12

Figure 5: Multicomponent sparse signal. First component estimation (a), (b); Second component (c), (d); Third component (e), (f). Missing values in time-frequency representations (a), (c) and (e) are presented in white color. 14

Figure 6: Top - The original SAR image; Bottom - The zoomed in SAR image. 16

Figure 7: Rotation rate of the antenna (a) at the range cell 123 and (b) at the range cell 124. 17

Figure 8: (a) Rotation rate of the main rotor blades and (b) Rotation rate of the tail rotor blades. 18

Figure 9: Simulated radar signals which correspond to a rigid body reflector with $\sigma_B = 1$ and a rotating reflector with reflection coefficient $\sigma_R = 0.8$: a) Absolute value of the STFT, b) Sorted STFT values, c) The original FT, and d) The reconstructed FT. Simulated radar signals which correspond to a rigid body reflector with $\sigma_B = 1$ and a rotating reflector with reflection coefficient $\sigma_R = 15$: e) Absolute value of the STFT, f) Sorted STFT values, g) The original FT, and g) The reconstructed FT. 23

Figure 10: The FT of a sinusoidal signal: (a) Original, (b) Reconstructed by summing 75% of the smallest STFT values, for each k, (c) Reconstructed by summing 50% of the smallest STFT values, (d) Reconstructed by summing 25% of the smallest STFT values. . . . 26

Figure 11: Sorted STFT values, $|\Psi_k(m)|$, with a colorbar (upper). The values of $A(m)$, obtained by summing the squared values of the sorted STFT along the frequency, with the adaptive threshold R_L obtained based on the average value of 10% of its smallest values - thick horizontal line (lower). 28

Figure 12: (a) The STFT of a signal consisting of one rigid body component and four sinusoidally modulated components. (b) The sorted STFT of the same signal. (c) The original FT of the signal. (d) The FT of rigid body, reconstructed by summing the STFT values remaining after sorting and eliminating samples that correspond to the m-D effect. 31

Figure 13: (a) The STFT of a signal consisting of five rigid body components and five sinusoidally modulated m-D components (b) The sorted STFT of the same signal. (c) The original FT of the signal. (d) The FT of rigid body, reconstructed by summing the STFT values remaining after sorting and eliminating samples that correspond to the m-D effect. 32

Figure 14: (a) The STFT of a simulated signal of a German Air Force Bell UH-1D Helicopter. (b) The sorted STFT of this signal. (c) Original FT of the signal. (d) The FT of the rigid body, reconstructed by summing the lowest absolute STFT values. (e) The FT of the rigid body, reconstructed by the proposed method. 34

Figure 15: (a) The STFT of a signal consisting of two very close components with constant frequency and one sinusoidally modulated component. (b) The sorted STFT of the same signal. (c) The original FT of the signal. (d) The FT of rigid body, reconstructed by summing the lowest STFT values. 35

Figure 16: Mean absolute error as a function of noise variance calculated for the case of one rigid body reflector without m-D. The solid line corresponds to the proposed method, while the dashed line corresponds to the full FT. 36

Figure 17: One rigid body reflector and one m-D reflector. Noiseless case (a–d): (a) The STFT absolute value, (b) Sorted STFT, (c) The original FT, (d) Reconstructed FT. A realization of noisy case with $\sigma_\varepsilon^2 = 4.5$ (e–h): (e) The STFT absolute value, (f) Sorted STFT, (g) The original FT, (h) Reconstructed FT. (i) Mean absolute error as a function of noise variance in 1000 noisy realizations. 38

Figure 18: One rigid body reflector and one close m-D reflector. Noiseless case (a–d): (a) The STFT absolute value, (b) Sorted STFT, (c) The original FT, (d) Reconstructed FT. A realization of noisy case with $\sigma_\varepsilon^2 = 4.5$ (e–h): (e) The STFT absolute value, (f) Sorted STFT, (g) The original FT, (h) Reconstructed FT. (i) Mean absolute error, in 1000 noisy realizations, as a function of noise variance. 39

Figure 19: Accelerating rigid body with a complex form of the mD. (a) TFR of the signal without motion compensation. (b) Sorted TFR of the original signal. (c) Original FT of the analysed signal. (d) Reconstructed FT of the accelerating rigid body without motion compensation. (e) TFR of the signal after motion compensation. (f) Sorted TFR of acceleration compensated signal. (g) The FT of the original signal with motion compensation. (h) Reconstructed FT of the accelerating rigid body with motion compensation. . . 41

Figure 20: Real radar data corresponding to a rigid body and three corner reflectors rotating at ~ 60 RPM (a–d). (a) the STFT. (b) Sorted STFT. (c) The original FT and (d) the FT reconstructed by summing over 50% of the lowest STFT samples. The same procedure is repeated for real radar data corresponding to a stronger rigid body and two corner reflectors rotating at ~ 40 RPM (e–h). A logarithmic amplitude scale is used in subplots (g) and (h). 42

Figure 21: Virtual Instrument – main screen 45

Figure 22: Load 1D external data 46

Figure 23: Load 2D external data 48

Figure 24: Time-frequency representation of the analyzed data 49

Figure 25: L-statistics analysis 50

Figure 26: Micro-Doppler parameter estimation results 51

Figure 27: Micro-Doppler parameters 51

Figure 28: Micro-Doppler parameter estimation results – multicomponent case – second analyzed component 52

Figure 29: Micro-Doppler parameters for second component in multi-component case 53

Figure 30: Range bin selection with 2D input data 54

Figure 31: Range bin selection with 2D input data 54

Figure 32: Time-frequency analysis toolbox demo. 56

Figure 33: Short-Time Fourier Transform of the analyzed signal. 57

Figure 34: S-method of the analyzed signal. 58

Figure 35: Advanced visualization options. 59

1 Introduction

If a target or any structure on a target has mechanical vibration or rotation in addition to its bulk translation, it might induce a frequency modulation on the returned signal that generates sidebands about the target's Doppler frequency shift. This is called the micro-Doppler (m-D) effect [1–10]. Radar signals returned from a target that incorporates vibrating or rotating structures, such as propellers of a fixed-wing aircraft, rotors of a helicopter, or the engine compressor and blade assemblies of a jet aircraft, contain m-D characteristics related to these structures [1, 2, 5, 9]. The m-D effect enables us to determine the dynamic properties of the target and it offers a new approach for the analysis of target signatures.

Micro-Doppler effect appears in the SAR/ISAR image of a target whenever the target has one or more rotating or vibrating parts. If the frequency modulations on the returned signal caused by the moving parts are not filtered, then the m-D effect can introduce distortion in the SAR/ISAR images [1,2,5,9]. The observation of very large distortions from experimental SAR/ISAR data has been reported. On the other hand, the m-D effect also carries information about the features of moving parts of a target that are complementary to existing target recognition methods. Several papers have been written about the ways to deal with the m-D effect. The wavelet analysis of the helicopter and human data, along with the time-frequency (TF) representation based imaging system, is presented in [1, 2]. Details on the physics of the m-D effect, with some typical examples, are given in [1–9]. A method for separating the m-D effect from the radar image, based on the chirplet transform, is proposed in [2, 10]. It is easier to estimate these features if the m-D effect is separated from the rigid body part of the radar image. Thus, the extraction of m-D effects is an important problem in the radar imaging. Since the spectral content of the signal corresponding to m-D effects is time-varying, time-frequency (TF) analysis techniques are an appropriate tool for the m-D features analysis and extraction [1–28].

The most common and simplest form of the signal that corresponds to the m-D effect is a sinusoidal frequency-modulated (FM) signal. This kind of the m-D signatures can be extracted based on the inverse Radon transform of its TFR [5]. This transform projects a two-dimensional (2D) sinusoidal signature into a single point whose position corresponds to the parameters of the sinusoidal signature. The technique based on the inverse Radon transform can be used for other nonsinusoidal periodic m-D forms. In general, the m-D effect, as a nonstationary signal with time-varying spectral content, can be separated from the rigid body by using the L-statistics on the TF signal representations [5]. The L-statistics based separation of the m-D effects from the rigid body is very efficient and simple for any m-D form. The Viterbi algorithm can improve the m-D tracking in high noise environments [4].

In Section 2, a method for the estimation of m-D motion parameters is provided. In this section, the inverse Radon transform is reviewed and the methodology is provided for m-D motion parameters estimation. Its application to the cases, with a fraction of period of the m-D signal being available, is presented. Since, the m-D is not necessary of the form of a sinusoidal frequency modulated (FM) signal, a simple algorithm for period estimation of a general form of the periodic signals is presented in this Section, as well. The m-D must be separated from a rigid body in order to be further analyzed, thus the L-statistics based algorithm for the m-D separation is presented in Section 3. The m-D toolbox based on L-statistics, spectrogram, and inverse Radon transform is given in Section 4. This toolbox will scan and search any m-D activity in the desired area of the SAR/ISAR image. The toolbox will have three options; 1) Focus the stationary target if there is no m-D, 2) Focus the target after removing the m-D, and 3) extract the m-D and determine the motion parameters such as rotation/vibration rate, initial phase, and amplitude of the stationary and moving targets. The toolbox was tested and validated against a variety of simulated and measured targets. In Section 4, the time-frequency toolbox is also illustrated. Conclusions are given in Section 5.

2 Estimation of micro-Doppler motion parameters

The m-D can be used to determine properties of a target [1–28], since the m-D parameters are related to the parameters of the corresponding micro-motions. Therefore, the radar m-D signatures are of a great potential for identifying properties of unknown targets. The most common form of the m-D is a form of sinusoidal frequency modulated (FM) signal.

Sinusoidally modulated signals appear in many applications, like in radars and communications. In the radar signal processing, the fast rotating, vibrating or oscillating parts reflect a signal causing m-D effect in a form of sinusoidally modulated signal. In practice it is very important to extract, decompose, and estimate parameters of these kinds of signals, since they are easily related to the physical dimensions and other properties of the moving objects.

In this section, we will present a method for analysis of sinusoidally modulated components based on the inverse Radon transform of signal's time-frequency representation. The Radon transform, widely used in computer imaging applications, is also used in time-frequency for projecting Wigner distribution in order to detect linear frequency modulated signals [33–37]. Here, we will use the inverse Radon transform rather than the Radon transform. Note, that the behavior of the direct and inverse Radon transform is completely different, in contrast, for example, to the Fourier transform [38]. Since the Radon transform of a two-dimensional signal containing

a two-dimensional delta function is a sinusoidal pattern with amplitude corresponding to the distance of the point from the origin and the initial phase corresponding to the phase of the point position, then it is obvious that a sinusoidal pattern in the time-frequency plane (produced by a time-frequency representation of sinusoidally modulated signal) will project to a two-dimensional delta in the inverse Radon transform. This is obviously an optimal transform for a two-dimensional sinusoidal pattern, since all signal energy from the time-frequency domain will be projected in a single point in the inverse Radon transform domain. The method will be introduced on monocomponent sinusoidally modulated signal. Then it will be extended to noisy and multicomponent signals that include one or more sinusoidal patterns. Finally the method will be applied to periodic and non-periodic patterns that are not produced by a sinusoidally modulated signals at all. The examples illustrate the efficiency of the presented method.

2.1 Radon and inverse Radon transform

A projection of a two-dimensional function $f(x, y)$ onto the x-axis is

$$R_f(x) = \int_{-\infty}^{\infty} f(x, y)dy. \tag{1}$$

A rotated version of a two-dimensional signal may be described in a rotated coordinate system, by a coordinate rotation transform. For an angle α, it reads

$$\begin{bmatrix} \xi \\ \zeta \end{bmatrix} = \begin{bmatrix} \cos(\alpha) & \sin(\alpha) \\ -\sin(\alpha) & \cos(\alpha) \end{bmatrix} \begin{bmatrix} x \\ y \end{bmatrix}.$$

The projection of a function $f(x, y)$ onto ξ, with a varying rotation angle α, is the Radon transform of the signal $f(x, y)$

$$R_f(\xi, \alpha) = \int_{-\infty}^{\infty} f(\xi, \zeta)d\zeta = \int_{-\infty}^{\infty}\int_{-\infty}^{\infty} f(\lambda, \zeta)\delta(\lambda - \xi)d\lambda d\zeta. \tag{2}$$

Let us consider simple setup where the analyzed image is two-dimensional delta function located at the point $f(x, y) = \delta(x - x_0)\delta(y - y_0)$ in x, y domain. Projection of $f(x, y)$ onto x axis is

$$R_f(x, 0) = \int_{-\infty}^{\infty} f(x, y)dy = \delta(x - x_0).$$

For an arbitrary direction $\xi_0 = x_0 \cos(\alpha) + y_0 \sin(\alpha)$, $\zeta_0 = -x_0 \sin(\alpha) + y_0 \cos(\alpha)$, the function $f(\xi, \zeta) = \delta(\xi - \xi_0)\delta(\zeta - \zeta_0)$ results in the Radon transform

$$\begin{aligned} R_f(\xi, \alpha) &= \int_{-\infty}^{\infty} f(\xi, \zeta) d\zeta = \delta(\xi - \xi_0) \\ &= \delta(\xi - (x_0 \cos(\alpha) + y_0 \sin(\alpha))). \end{aligned} \tag{3}$$

Note that this is a sinusoidal pattern in a two-dimensional (ξ, α) domain, with the amplitude $\sqrt{x_0^2 + y_0^2}$ and the phase $\psi = \arctan(y_0/x_0)$. Of course, the Radon transform is periodic in α with 2π. Projections for $0 \leq \alpha < \pi$ are sufficient to calculate all transform values. By knowing all the projections, for $0 \leq \alpha < \pi$, we can calculate the two-dimensional Fourier transform of $f(x, y)$. It means that we can reconstruct a two-dimensional function $f(x, y)$ from its projections or integrals (basic theorem for computed tomography). The inverse Radon transform may be calculated in the Fourier domain or by projecting back the Radon transform (back-projection method). Thus, a point in the (x, y) domain transforms to a sinusoidal pattern in Radon transform domain. It means that a sinusoidal pattern will be transformed into a point by using the inverse Radon transform (IRT). When all energy is concentrated into a point, then its parameters estimation is very robust and reliable.

2.2 Parameters estimation

Let us now consider sinusoidally frequency modulated signal

$$x(t) = A_x \exp\left(j \frac{A_m}{f_m} \sin(2\pi f_m t + \theta_m)\right). \tag{4}$$

It is known that a time-frequency representation $T(t, \omega)$ of a given signal concentrate the signal energy along the signal instantaneous frequency

$$\omega_i(t) = 2\pi A_m \cos(2\pi f_m t + \theta_m)$$

i.e., this signal in (t, ω) plane is presented as sinusoidal pattern image (with more or less deviations depending on the time-frequency representation used to transform the signal into time-frequency domain). If we change the time coordinate with $\varphi = 2\pi f_m t$ then, from the previous section we can conclude that the IRT of the obtained image $T(\varphi/(2\pi f_m), \omega)$ reduces to single point where distance from origin correspond to modulation parameter A_m, and the angle of the point is equal to θ_m. In this way, we can accurately estimate modulation parameters A_m and θ_m.

The modulation parameter f_m can be estimated in the following way. Let us introduce coordinate change from t to φ as $\varphi = \alpha t$ where α is a parameter. Now we can vary

the parameter α within some range of possible values and search for the value $\hat{\alpha}$ that produces single point IRT. In that case we know that $\hat{\alpha} = 2\pi f_m$ and we can estimate the modulation parameter f_m. In this procedure, it is needed to find the value of α when the IRT reduces to a single point within the considered domain. This mean that the IRT is ideally concentrated and the concentration measures [35] can be used to detect that we reached $\hat{\alpha}$. The range for α should be wide enough to include $2\pi f_m$. Its limits could be determined as the minimal and the maximal expected $2\pi f_m$ in the considered case.

The estimation algorithm is summarized as:

Step 1. Start from a frequency modulated signal $x(t)$ with unknown modulation parameters. Assume that the modulation frequency satisfies $f_{\min} \leq f_m \leq f_{\max}$, where $f_{\min}$ and $f_{\max}$ are constants.

Step 2. Calculate the time-frequency representation $T(t, \omega)$ of $x(t)$. Here we can use any time-frequency representation [8] concentrating the signal energy along the instantaneous frequency in the time-frequency plane. The result of this step is a two-dimensional time-frequency image of the considered signal.

Step 3. Consider a set of possible α as M equally spaced values between $2\pi f_{\min}$ and $2\pi f_{\max}$.

Step 4. For each a within the considered set, introduce coordinate change $\varphi = \alpha t$ and calculate the IRT of the image $T(\varphi/\alpha, \omega)$.

Step 5. Calculate the concentration measure μ of the obtained IRT for each α and find $\hat{\alpha}$ that provide the highest concentration.

Step 6. Estimate the modulation frequency as $\hat{f}_m = \hat{\alpha}/(2\pi)$.

Step 7. Find the position of IRT maximum calculated with $\alpha\hat{}$, i.e., IRT of $T(\varphi/\alpha\hat{}, \omega)$. Denote the detected coordinates as x_m and y_m.

Step 8. Estimate the modulation amplitude as

$$\hat{A}_m = \sqrt{x_m^2 + y_m^2}.$$

Step 9. Estimate the modulation phase as $\hat{\theta}_m = \arctan \frac{y_m}{x_m}$.

In the case of non-sinusoidally modulated signals, producing non-sinusoidal patterns in the time-frequency plane, the presented approach will produce the closest sinusoidal pattern form, as it will be shown in examples.

2.3 Method implementation

We use the spectrogram and the S-method as time-frequency representations in the algorithm Step 2. The spectrogram is defined as a squared modulus of the short-time Fourier transform. In the discrete time domain, it reads

$$SPEC(n,k) = |STFT(n,k)|^2$$
$$STFT(n,k) = \sum_{m=0}^{N_w} w(m)x(n+m)e^{-j\frac{2\pi}{N_w}mk},$$

where $w(n)$ is the analysis window of the length N_w. Along with the spectrogram, we will use the S-method as a time frequency representation. The discrete S-method is of the form

$$SM(n,k) = |STFT(n,k)|^2 + 2\,\mathrm{Re}\left[\sum_{p=1}^{L} STFT(n,k+p)STFT^*(n,k-p)\right],$$

where beside the time-domain window, used in the STFT calculation, we have a parameter L that corresponds to the number of spectrogram correcting terms [8]. It is known that the S-method can produce highly concentrated time-frequency representation of a given signal. The S-method is numerically very efficient since there is no need for signal oversampling. Two special cases of the S-method are the spectrogram (with $L = 0$) and the pseudo Wigner distribution (with $L = N_w/2$).

The concentration measure is needed in the algorithm, Step 5. Here we use the normalized measure

$$\mu = \frac{\mathcal{M}_1^1}{\mathcal{M}_{1/2}^{1/2}}$$

where $\mathcal{M}_p^p$ is defined in [35] as

$$\mathcal{M}_p^p = \left(\sum_n \sum_k |T(n,k)|^{1/p}\right)^p$$

and $T(n,k)$ are the discrete samples of a non-negative part of the IRT.

Example 1: Consider $N = 129$ samples of noise free FM signal (4) sampled with $t = n\Delta t$, $\Delta t = 1/128$, $n = 0, 1, \ldots N-1$. The signal parameters are $A_x = 1$, $f_m = 1.4$, $A_m = 50$ and $\theta_m = 30°$ The spectrogram and the S-method of the considered signal are presented in Figure 1(a) and (b). The spectrogram is calculated with a 17-point Hann window, while the S-method is calculated with a 55 point Hann window and $L = 8$. In both cases, the time-frequency representation is calculated at each available

time instant (i.e., with overlapping). The parameter α is varied from 0.2 to 15 with step 0.2. For each α, the IRT along with the corresponding concentration measure is calculated. The concentration measure $\mu(\alpha)$ is presented in Figure 1 (c) and (d), where the minimum of this measure (i.e., highest concentration) is depicted by a circle.

Figure 1(e) and (f) present the IRT obtained for $\hat{\alpha} = 8.8$. The maximum position in the IRT is determined and the modulation parameters are estimated in the spectrogram case as

$$\hat{f}_m = \frac{8.8}{2\pi} \approx 1.4, \quad \hat{A}_m = 49.1, \quad \hat{\theta}_m = 31.4^\circ$$

and in the S-method case as

$$\hat{f}_m = \frac{8.8}{2\pi} \approx 1.4, \quad \hat{A}_m = 48.1, \quad \hat{\theta}_m = 32.2^\circ$$

As we can see in both cases. the modulation parameters are very close to true values. It means that the method will not be too sensitive with respect to the time-frequency representation.

The IRT for $\alpha = 7$ (in the spectrogram case) and $\alpha = 10$ (in the S-method case) are given in Figure 1(g) and (h). These subplots illustrate that the IRT for optimal α (subplots (c) and (d)) is better concentrated than the IRT with another α.

Example 2: The estimation procedure is applied to a noisy signal $s(n\Delta t) = x(n\Delta t) + \varepsilon(n)$, where the noise $\varepsilon(n)$ is a complex white Gaussian noise with $SNR = 0\,\text{dB}$. The results are presented in Figure 2(a) and (b). The spectrogram of $s(n)$ is presented in Figure 2(a), while the concentration measure of the IRT, for various α, is given in Figure 2(b). In the spectrogram calculation, the number of frequency points is 101, i.e., windowed signal is zero-padded prior to the DFT calculation. Based on the IRT obtained for optimal α (denoted by circle in Figure 2(b)), the modulation parameters are estimated as

$$\hat{f}_m = \frac{8.8}{2\pi} \approx 1.4, \quad \hat{A}_m = 49.1, \quad \hat{\theta}_m = 30.2^\circ$$

and the resulting sinusoidal modulation is plotted over the spectrogram with a black line Figure 2(a). The estimated parameters are very close to the parameters estimated for noisy free case.

A multicomponent signal composed from a sinusoidally FM component (the same as in Example 1), a linear FM component, and a constant frequency component,

$$s(t) = x(t) + 0.6\exp\left(j40\pi(t-0.8)^2\right) + 0.6\exp(j50\pi t)$$

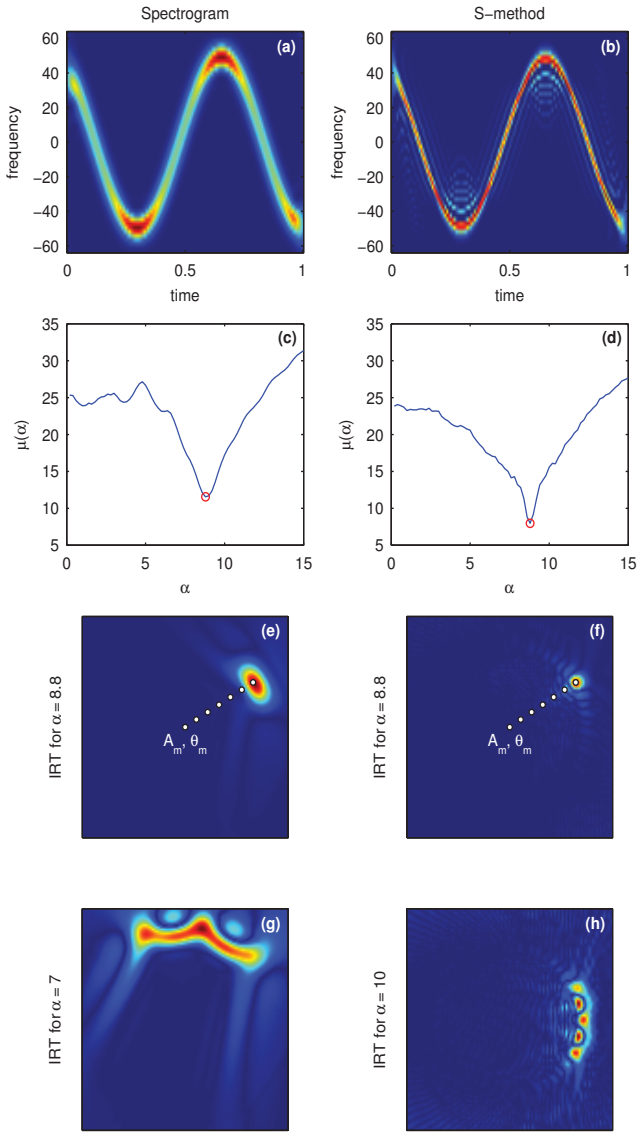

Figure 1: *Modulation parameters estimation for the mono-component non-noisy sinusoidally FM signal. Time frequency representation (a), (b); concentration measure (c), (d); inverse Radon transform with highest concentration (e), (f) and inverse Radon transform when the parameter α is not optimally chosen (g), (h).*

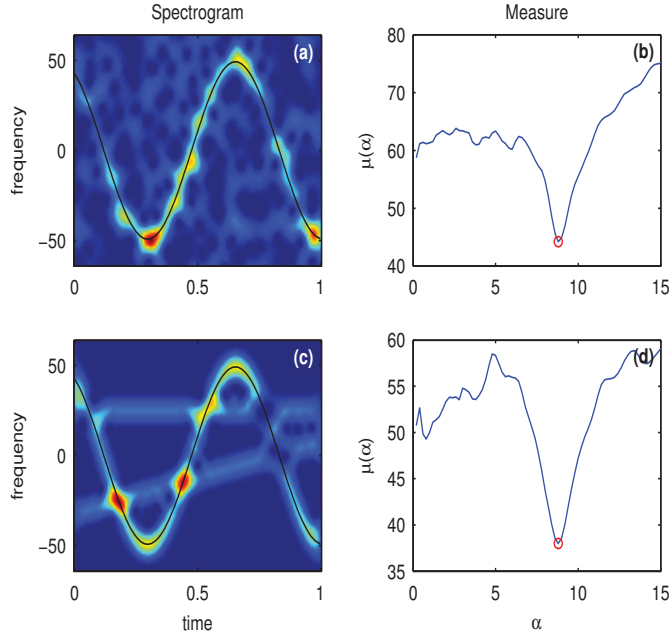

Figure 2: *Parameter estimation of the noisy signal with* $\mathrm{SNR} = 0\,\mathrm{dB}$ *(a), (b) and the multicomponent signal (c), (d). Estimated modulation is plotted with black line over the spectrogram image.*

is considered. The results obtained with the proposed procedure are presented in Figure 2(c) and (d). Estimated parameters are

$$\hat{f}_m = \frac{8.8}{2\pi} \approx 1.4, \quad \hat{A}_m = 49.1, \quad \hat{\theta}_m = 30.2^\circ.$$

From this example, we see that the proposed method is robust to the noise and some other possible interferences.

2.4 Multicomponent signal analysis

This approach may be generalized to a multicomponent signal

$$x(t) = \sum_{k=1}^{K} A_x^{(k)} \exp\left(j \frac{A_m^{(k)}}{f_m^{(k)}} \sin(2\pi f_m^{(k)} t + \theta_m^{(k)}) \right) + \varepsilon(t), \tag{5}$$

where $\varepsilon(t)$ denotes disturbing components and noise. Two scenarios are possible. One is that in the application of the previous algorithm, in Step 5, the concentration measure μ of the obtained IRT produces at once several or all K values of α with visible and distinguishable concentration measure peaks. Then, these values are associated to the corresponding signal parameters, as in Steps 6-9. However, due to different amplitudes and different number of periods in the time-frequency plane usually only the strongest component is visible in the concentration measure. In this case, its

parameter $\hat{\alpha}$ is estimated as in Step 5. Other parameters are estimated for this component as in Steps 6-9. The strongest component is removed and the algorithm is used on the remaining signal components, until the energy of the remaining signal is negligible. After parameters of all components are found, they can be readjusted by a mean-squared comparison with the original signal.

Example 3: Let us consider a multicomponent noisy signal consisted of $K = 3$ sinusoidally FM components of the form (5). Signal parameters are:

$A_x^{(1)} = 1$, $f_m^{(1)} = 1.4$, $A_m^{(1)} = 50$, $\theta_m^{(1)} = 30°$,

$A_x^{(2)} = 0.7$, $f_m^{(2)} = 1$, $A_m^{(2)} = 35.7$, $\theta_m^{(2)} = -60°$,

$A_x^{(3)} = 0.7$, $f_m^{(3)} = 0.8$, $A_m^{(3)} = 28.6$ and $\theta_m^{(3)} = 180°$.

The proposed method estimates parameters of one component, as presented in Figure 3(a) and (b). The estimated parameters are

$$\hat{f}_m^{(1)} = \frac{8.8}{2\pi} \approx 1.4, \quad \hat{A}_m^{(1)} = 48.8, \quad \hat{\theta}_m^{(1)} = 29.6°$$

From Figure 3(a), we can see that estimated modulation parameters highly correspond to the component instantaneous frequency. Now we will filter out the estimated component.

In the filtering procedure, the original signal is demodulated

$$x_d(n) = x(n) \exp\left(-j\frac{\hat{A}_m}{\hat{f}_m} \sin(2\pi \hat{f}_m n\Delta t + \hat{\theta}_m)\right).$$

The DFT of the demodulated signal $X_d(k) = \text{DFT}[x_d(n)]$ is calculated and DC component is removed by putting zero value to $X_d(0)$, and several neighboring points $X_d(1)$, $X_d(N)$, $X_d(2)$, $X_d(N-1)$, etc. Here the signal length is $N = 129$ and we remove 7 points. The filtered signal is obtained by the inverse DFT $x_f(n) = \text{IDFT}[X_d(k)]$.

Finally filtered signal is modulated in order to cancel frequency shifts in the remaining components caused by the demodulation

$$x_m(n) = x_f(n) \exp\left(j\frac{\hat{A}_m}{\hat{f}_m} \sin(2\pi \hat{f}_m n\Delta t + \hat{\theta}_m)\right).$$

Now we can repeat the estimation procedure with $x(n) = x_m(n)$ and estimate the second component parameters. The results are presented in Figure 3(c) and (d). The

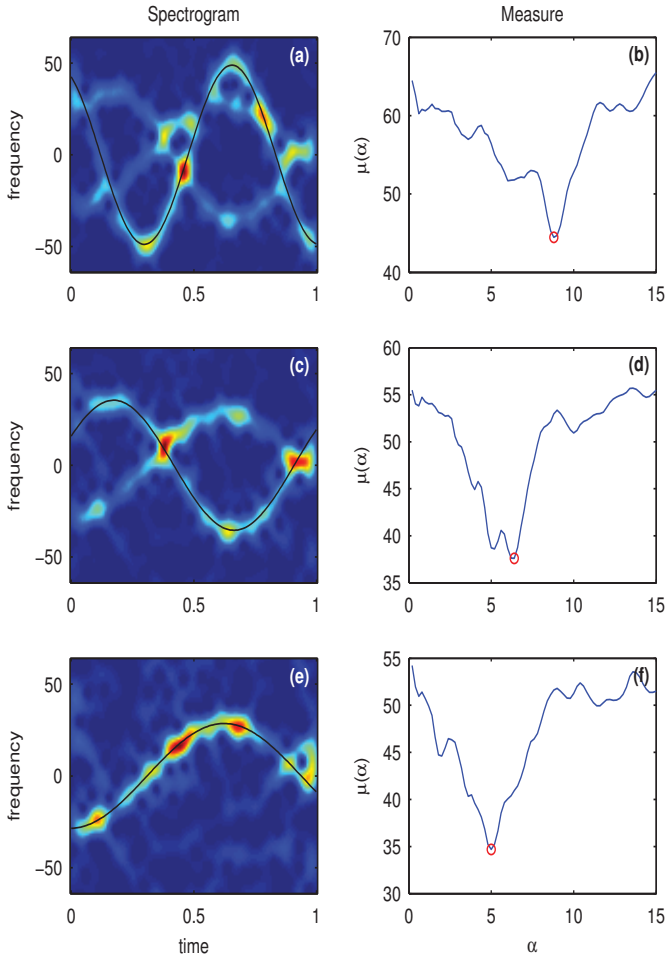

Figure 3: *Multicomponent signal. Estimation of the first component (a), (b); the second component (c), (d); and the third component (e) and (f). Each component is removed from the signal after the estimation, according to the described procedure, prior to next component estimation.*

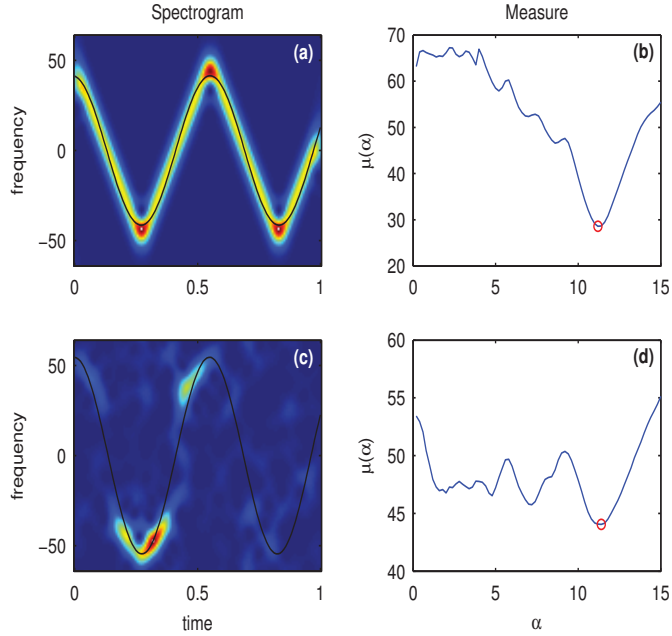

Figure 4: *Nonsinusoidal modulation. Triangulary modulated signal (a), (b); Signal with nonsinusoidal modulation and varying amplitude (c), (d).*

estimated modulation parameters are

$$\hat{f}_m^{(2)} = \frac{6.4}{2\pi} \approx 1.02, \quad \hat{A}_m^{(2)} = 35.4, \quad \hat{\theta}_m^{(2)} = -63.4^\circ$$

In the next step, we filter the estimated component and proceed to the parameters estimation for the last component. Results are given in Figure 3(e) and (f) and the estimated parameters are

$$\hat{f}_m^{(3)} = \frac{5}{2\pi} \approx 0.796, \quad \hat{A}_m^{(3)} = 28.5, \quad \hat{\theta}_m^{(3)} = -178.7^\circ.$$

The agreement with the true parameters is high.

2.5 Nonsinusoidally modulated signals

The presented estimation procedure could be used even if the analyzed signal is periodic, but not sinusoidally modulated. We will illustrate this application on an example.

Example 4: Considered a triangularly modulated signal $x_1(t)$ and nonsinusoidal periodic modulated signal $x_2(t)$ with a varying amplitude

$$x_1(t) = \exp\left(j \int_0^t 200 \arcsin(\cos(3.6\pi u))du\right)$$

$$x_2(t) = A(t) \exp\left(j \int_0^t 300 \sqrt[3]{\arcsin(\cos(3.6\pi u))}du\right)$$

where

$$A(t) = \exp\big(-\big(\tfrac{t-0.35}{0.3}\big)^2\big).$$

Although the proposed method is derived having in mind the sinusoidal modulation, the results presented in Figure 4 clearly show that the applicability of the proposed method is not limited to the sinusoidal modulation patterns only. The estimated modulation parameters for signal $x_1(t)$ are

$$\hat{f}_m = \frac{11.2}{2\pi} \approx 1.78, \quad \hat{A}_m = 41.4, \quad \hat{\theta}_m = 6.1^\circ$$

and for signal $x_2(t)$

$$\hat{f}_m = \frac{11.4}{2\pi} \approx 1.81, \quad \hat{A}_m = 54.5, \quad \hat{\theta}_m = 1.33^\circ.$$

They agree with $f_m = 1.8$ in the considered signals. The closest estimated sinusoids are presented in this figure as well.

2.6 Analysis using partial data

Assume that not all signal samples is available. In this case, we can calculate the spectrogram only at time instants/intervals when signal samples $x(n)$ are available. This procedure will be illustrated with an example.

Example 5: Consider the signal defined in Example 3, and assume that samples from intervals 20-28, 50-80, and 95-110 are missing. Since the total number of samples is 129 we have 43% of missing samples. The estimation results obtained by using the available signal values are presented in Figure 5. Regions with unavailable samples are presented with white color in this figure. The parameters estimated using available samples are

$$\begin{aligned}
\hat{f}_m^{(1)} &= \frac{6.4}{2\pi} \approx 1.401, \quad \hat{A}_m^{(1)} = 49.4, \quad \hat{\theta}_m^{(1)} = 30.8^\circ \\
\hat{f}_m^{(2)} &= \frac{6.4}{2\pi} \approx 0.986, \quad \hat{A}_m^{(2)} = 35.0, \quad \hat{\theta}_m^{(2)} = -58.3^\circ \\
\hat{f}_m^{(3)} &= \frac{6.4}{2\pi} \approx 0.796, \quad \hat{A}_m^{(3)} = 28.5, \quad \hat{\theta}_m^{(3)} = -178.7^\circ.
\end{aligned}$$

Even with a reduced number of available signal values, the presented method produced accurate estimates.

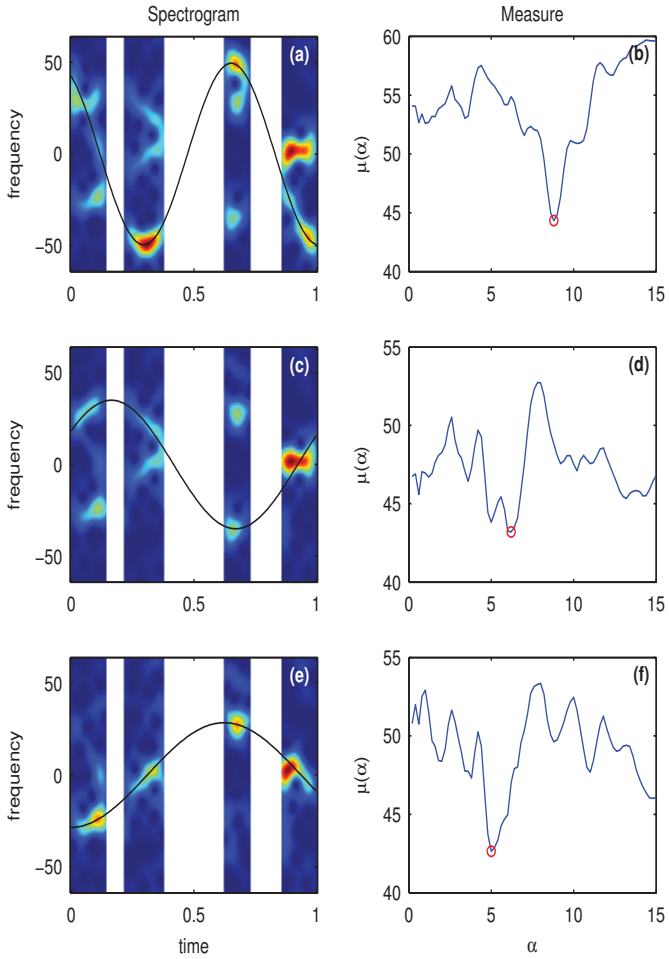

Figure 5: *Multicomponent sparse signal. First component estimation (a), (b); Second component (c), (d); Third component (e), (f). Missing values in time-frequency representations (a), (c) and (e) are presented in white color.*

2.7 Experimental data: rotating antenna in SAR

Radar returns were collected from a rotating antenna using a APY-6 radar in a SAR scenario [2]. Using these data sets, the m-D features relating to a rotating antenna were extracted. The m-D features for such rotating targets may be seen as a sinusoidal phase modulation of the SAR azimuth phase history. The phase modulation may equivalently be seen as a time-varying Doppler frequency.

Figure 6a shows the original SAR image and Figure 6b displays the zoomed in SAR image between the range cells 115 and 130. The Doppler smearing due to the rotating parts is often well localized in a finite number of range cells. It is reasonable to process the Doppler signal for each range cell independently. Since the prior information about the location of the target is known, the data at the range cells 123 and 124 were analyzed. The micro-Doppler toolbox, which is presented in Section 4 was used to estimate the rotation rate of the antenna. Figure 7 illustrates the m-D parameter estimation results. Figure 7a shows the rotation rate at range cell 123 and Figure 7b shows the rotation rate at range cell 124 The estimated rotation rate is 4.8 seconds, which is very close to the actual value of 4.7 seconds.

2.8 Experimental data: hovering helicopter

The experimental data used in the analysis that follows are of a hovering helicopter. For a helicopter, the main rotor blades, the tail rotor blades and the hub have unique signatures suitable for target identification [39–41]. Generally, radar returns from a helicopter are back-scattered from the fuselage, the rotor blades, the tail blades and the hub among other structures. The motion of the rotor blades depends upon the coupling between the aerodynamics and the rotor dynamics. Each blade is a rotating aerofoil having bending, flexing and twisting motion. The radar cross section of a segment of the blade depends upon its distance from the centre of rotation, its angular position and the aspect angle of the rotor [40]. For simplicity, the rotor blade can be modelled as a rigid, linear and homogeneous rod rotating about a fixed axis with a constant rotation rate.

The rotational motion of rotor blades in a helicopter imparts a periodic modulation on radar returns. The rotation-induced Doppler shifts relative to the Doppler shift of the fuselage (or body) occupy unique locations in the frequency domain. Whenever a blade has specular reflection such as at the advancing or receding point of rotation, the particular blade transmits a short flash to the radar return. The rotation rate of the rotor is directly related to the time interval between these flashes. The duration of a flash is determined by the radar wavelength and by the length and rotation rate of the blades. A flash resulting from a blade with a longer length and a radar with a shorter wavelength will have a shorter duration [1].

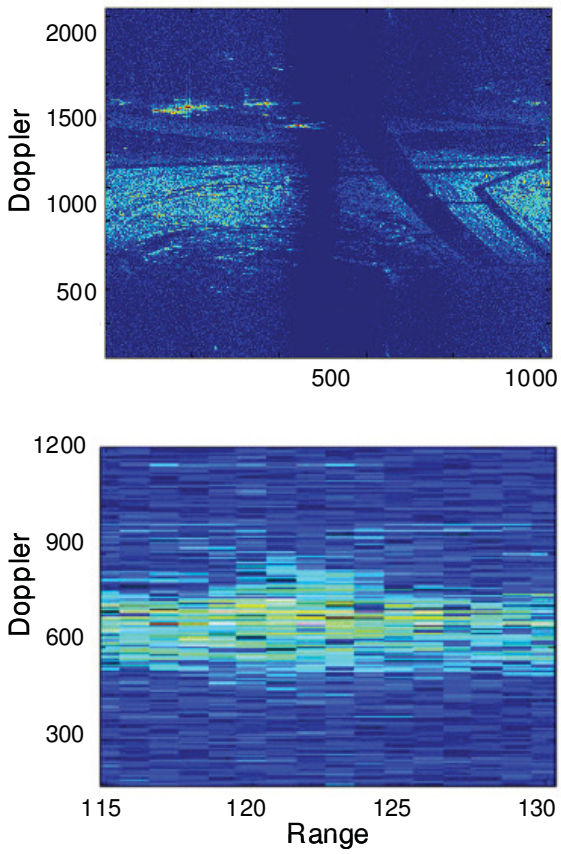

Figure 6: *Top - The original SAR image; Bottom - The zoomed in SAR image.*

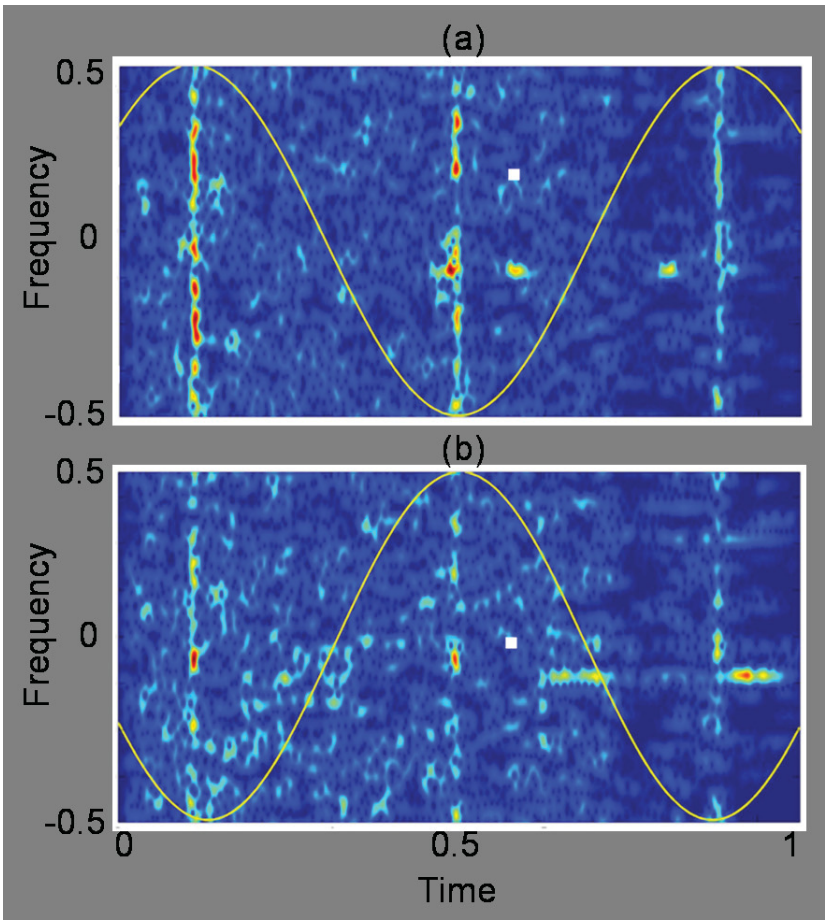

Figure 7: *Rotation rate of the antenna (a) at the range cell 123 and (b) at the range cell 124.*

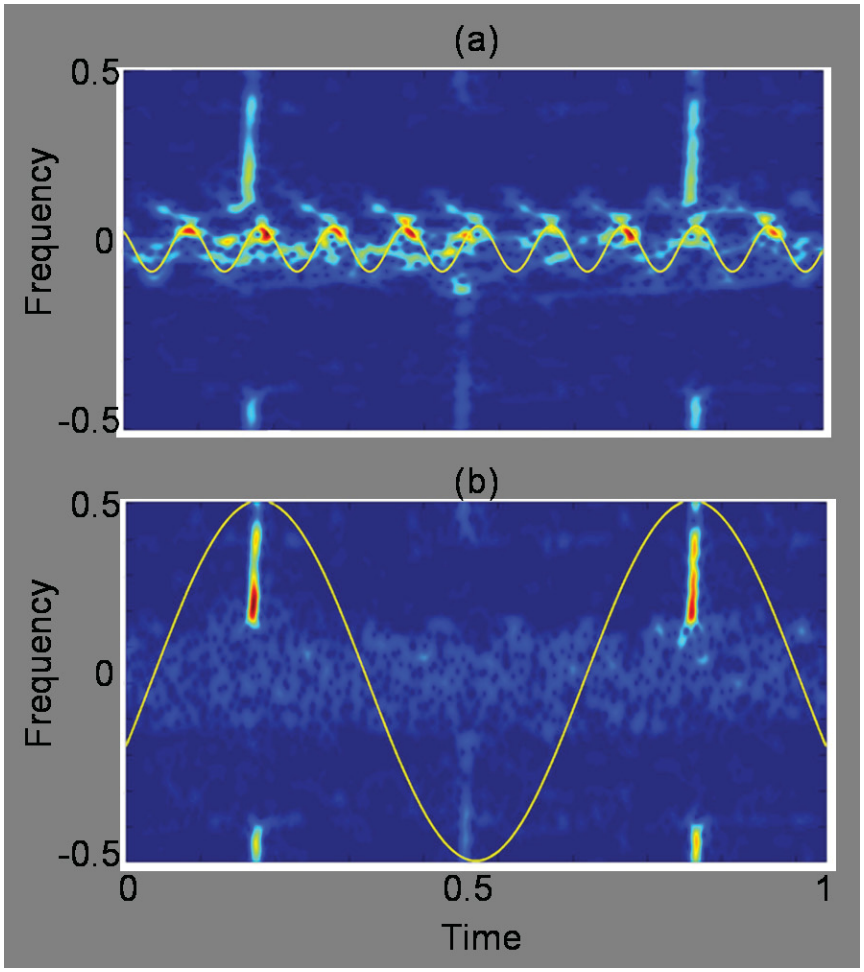

Figure 8: *(a) Rotation rate of the main rotor blades and (b) Rotation rate of the tail rotor blades.*

The helicopter employed in the experiment is hovering above the ground at a height of approximately 60 m and at a range of 2.5 km from the radar. The main rotor comprised five blades and the tail rotor consists of six blades. The m-D toolbox was used to estimate the rotation rates of the main and tail rotor blades of the helicopter. The rotation rate of the tail rotor blades is 1030 rpm (Figure 8a). The rotation rate of the main rotor blades is 203 rpm for this helicopter (Figure 8b). Both estimations are in agreement with the actual values.

3 Micro-Doppler removal in the radar imaging analysis

The m-D effect appears in the inverse synthetic aperture radar (ISAR) imaging when a target has one or more fast moving parts [2, 5, 7–9]. Similar effect appears in the synthetic aperture radar (SAR) imaging, as well, [2, 49].

In this report, we use the L-statistics based approach for the rigid body separation. In order to remove the m-D effect, we perform the TF analysis within the coherent integration time (CIT). In our previous approach [5], we used order statistics and several TF representations with various windows. The obtained TF representations were then used to make decision whether a component belongs to the rigid body or to the fast moving target point. Here, we use only one window function in the analysis. Order statistics is performed based on the spectrogram, while the rigid body signal synthesis is done in the complex TF domain. This approach is very simple to use and produces better results than the other approaches. It is also robust to the noise influence, since it uses the L-statistics, being known as a robust signal processing tool [51]. The L-statistics application to the complex STFT leads to a form of super-resolution representation, as well. It can separate very close rigid body components, even when that is not possible by using the standard Fourier transform (FT) over the entire CIT. The proposed method can be easily adapted for efficient compensation of a residual, uncompensated, rigid body acceleration in the presence of the m-D effects.

In order to improve the calculation efficiency, we have proposed a procedure to establish whether there is any target return in a considered range bin. Moreover, by bearing in mind that in the ISAR/SAR analysis only some range bins may contain the m-D effect, while most of the range bins are m-D free, in this report, we have defined a criterion for detecting ranges which contain the m-D effects. The m-D removal procedure could be performed only for these particular range bins.

3.1 Time-frequency analysis and L-statistics

A simpler way to localize the signal behavior in shorter intervals, within the CIT, is in applying a window function to the standard FT. The resulting short-time Fourier transform (STFT) is defined as

$$STFT(t,\Omega) = \int_{-\infty}^{\infty} s(\tau)w(\tau - t)e^{-j\Omega\tau}d\tau, \tag{6}$$

or in a discrete form

$$STFT(m,k) = \sum_{i=0}^{M-1} s(i)w(i-m)e^{-j2\pi ik/M}, \tag{7}$$

where $w(i)$ is a window function used to truncate the considered signal. The squared absolute value of the STFT is called the spectrogram. In most of the provided examples, we will use a Hanning window. The window width is M_w, $w(i) \neq 0$ for $-M_w/2 \leq i \leq M_w/2 - 1$. In our applications, the window is zero padded up to M, the same number of samples as in FT, so that we have the same frequency grid in the STFT as in the FT. Then, we can later easily reconstruct the FT, without interpolation, with the concentration close or equal to the concentration of the original FT. We know that, by using a lag window $w(i)$ in the STFT, the concentration in frequency is reduced, as compared to the original FT. For example, if the lag window width is M_w, then the concentration of a sinusoidal signal is reduced M/M_w times, i.e., the STFT-based ISAR/SAR image of a rigid body point (the main lobe of the FT of a sinusoid) would be approximately M/M_w times wider than the original FT based image of the same reflecting point. We will also refer to this effect as: the concentration being M/M_w times lower in the STFT than in the original FT.

3.1.1 Restoring the high FT concentration from the STFT

The concentration could be restored to the original one by summing all the low concentrated STFT (complex) values over m. Since we calculated $STFT(m,k)$ with the window of the width M_w, there are two possibilities for its summation: (a) For all time instants $0 \leq m \leq M-1$, when the signal $s(i)$ has to be zero-padded for $-M_w/2 \leq i < 0$ and $M \leq i < M + M_w/2 - 1$; (b) For instants $M_w/2 \leq m \leq M - M_w/2$, when zero-padding of $s(i)$ is not used. Reconstruction formula, for the

case when the signal is not zero-padded, is

$$\sum_{m=M_w/2}^{M-M_w/2} STFT(m,k) = \tag{8}$$
$$\sum_{i=0}^{M-1} s(i) \left[\sum_{m=M_w/2}^{M-M_w/2} w(i-m) \right] e^{-j2\pi ik/M}$$
$$= \sum_{i=0}^{M-1} s(i) w_1(i) e^{-j2\pi ik/M} = S_{w_1}(k).$$

In the case when the STFT is calculated for each time instant (time step one in the STFT calculation), the resulting window $w_1(i)$ is constant, $w_1(i) = const$, for $M_w - 1 \leq i \leq M - M_w$, for any window. It means that during the most of the CIT interval we have the normalized resulting window $w_1(i)$ being close to the rectangular one, with a small transition at the ending M_w points. The FT of the window obtained during the process of reconstruction produces a concentration very close to the full range rectangular window case (i.e., no window). It means that we will be able to reconstruct the FT with a concentration close to the one in the original FT, by using low concentrated STFTs, calculated with narrow windows. In this way, we will restore the high concentrated radar image, although we used low concentrated STFT in the analysis. The transition at the ending points of $w_1(i)$ can be easily overcome by zero padding the analyzed signal $s(i)$ with $M_w/2$ samples on both sides, (as explained before). Then, the pure rectangular window $w_1(i)$ would be obtained, for any window $w(i)$. The analysis is not restricted to the step one in the STFT calculation. The same resulting window would be obtained for a step equal to a half of the window width ($M_w/2$) and a Hann(ing), Hamming, triangular or rectangular window. The same is valid for steps equal to $M_w/4$, $M_w/8$, etc.

In order to explain how this mechanism of restoring the original concentration, by summing low-concentrated images, works, consider $s(t) = \exp(j\omega_0 t)$. Its FT is a delta pulse $S(\Omega) = 2\pi\delta(\Omega - \omega_0)$. The STFT of this signal produces

$$STFT(t,\Omega) = W(\Omega - \omega_0)\exp(j(\Omega - \omega_0)t). \tag{9}$$

Let us now analyze the result of summing the STFT values over t:

For $\Omega = \omega_0$, constant values of $W(0)$ will be integrated over an infinite time interval, with the phase $\exp(j(\Omega - \omega_0)t) = \exp(j0)$, producing $\int_{-\infty}^{\infty} STFT(t,\Omega)dt \to \infty$ for $\Omega = \omega_0$.

For any other Ω not equal to ω_0, i.e., when $\Omega = \omega_0 + \theta$, $\theta \neq 0$, we will have the integration $\int_{-\infty}^{\infty} W(\theta)\exp(j\theta t)dt = W(\theta)\int_{-\infty}^{\infty}\exp(j\theta t)dt = 0$. Therefore, all values

for $\Omega \neq \omega_0$ are averaged out to zero by summation of the low concentrated STFTs over time.

The discrete form of (9), is

$$S(k) = \sum_{m=0}^{M-1} W(k - k_0) e^{j2\pi m(k-k_0)/M} \tag{10}$$

with the same conclusions as in the continuous case. Values of $S(k)$, when the signal is not zero-padded, are close to (10).

3.1.2 Basic idea for the separation of a rigid body and fast rotating part

The presented mechanism of restoring the original concentration of the FT, in conjunction with the knowledge of the TF behavior patterns of fast moving and rigid scattering points, lead us to an algorithm for the m-D free, highly concentrated, radar image. The rigid body and the fast moving points behave differently in the TF representation of the returned radar signal, within the CIT. The rigid body signal is almost constant in time (stationary), while the fast-varying m-D part of the signal is highly non-stationary. This part of signal keeps changing its position in the frequency direction.

For the illustration, let us assume that the signal is returned from one point of a rigid body scatterer and one point of a fast rotating (m-D) scatterer. We analyze two cases with different strengths of the m-D reflection. In the first case, the reflection coefficient of the rigid body is $\sigma_B = 1$, while the reflection coefficient of the fast moving scatterer is $\sigma_R = 0.8$. The STFT representation of the resulting signal is shown in Figure 9(a). The second case is with a strong m-D, $\sigma_R = 15$ and the same σ_B as in the previous case. The STFT representation of this signal is shown in Figure 9(e). In both cases, the rigid body part is at a constant frequency for all t within the CIT, while the fast rotating part changes frequency. If we perform sorting over the time axis, as in Figure 9(b,f), we will not change the result of the summation in (8) since it is a commutative operation. By summing the STFT values over time, from either of these two plots, presented in Figure 9(a,b) or Figure 9(e,f), we will get the original FT of the corresponding signal Figure 9(c,g). Note that any value of σ_R from (and including the case without m-D) $\sigma_R = 0$ up to $\sigma_R \gg \sigma_B$ will not significantly change the pattern.

The basic idea for separating the rigid body and the fast rotating part is in the sorting of STFT values of the returned radar signal along the time axis, within the CIT. Since the rigid body return is stationary, the sorting procedure will not significantly change the distribution of its values. However, the fast-varying m-D part of the signal is

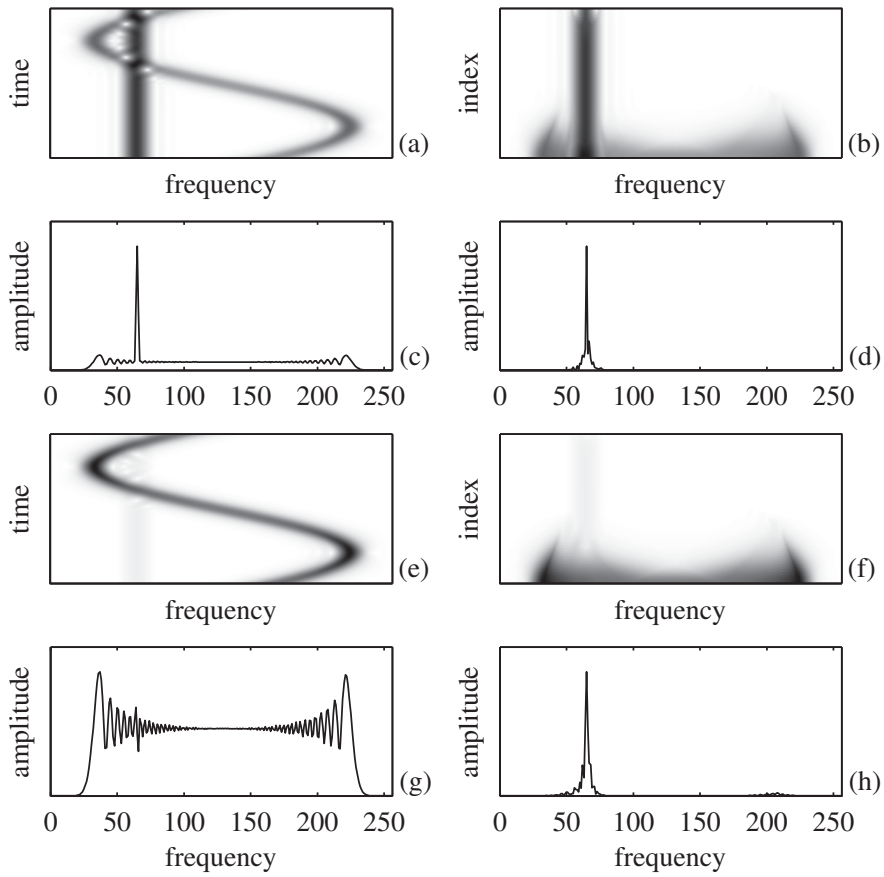

Figure 9: *Simulated radar signals which correspond to a rigid body reflector with* $\sigma_B = 1$ *and a rotating reflector with reflection coefficient* $\sigma_R = 0.8$*: a) Absolute value of the STFT, b) Sorted STFT values, c) The original FT, and d) The reconstructed FT. Simulated radar signals which correspond to a rigid body reflector with* $\sigma_B = 1$ *and a rotating reflector with reflection coefficient* $\sigma_R = 15$*: e) Absolute value of the STFT, f) Sorted STFT values, g) The original FT, and g) The reconstructed FT.*

highly non-stationary, occupying different frequency bins for different time instants (in the case of flashes it exists for some time-instants only). Its existence is short in time, for each frequency, over a wide range of frequencies. Thus, after sorting the STFT along the time axis, the m-D part of the signal has strong values over a wide frequency range, but for a few samples only. By removing several large amplitude values of the sorted STFT, for each frequency, we eliminate most or all of the m-D part of the signal. Summing the rest of the STFT values over time we will get the rigid body radar image. The sinusoidal m-D pattern, presented in Figure 9, is just an example of such a signal. This idea can be applied on any non-stationary signal form. The m-D part of a signal is non-stationary by definition.

Let us consider a set of M (or $M - M_w$ if the signal is not zero-padded) elements of the STFT, for a given frequency k,

$$\mathbf{S}_k(m) = \{STFT(m,k), m = 0, 1, ..., M-1\}.$$

After sorting $S_k(m)$ along the time, for a given frequency k, we obtain a new ordered set of elements $\Psi_k(m) \in S_k(m)$ such that $|\Psi_k(0)| \leq |\Psi_k(1)| \leq .... \leq |\Psi_k(M-1)|$. Of course, the addition is commutative operation, so if we use the whole set, we get

$$\sum_{m=0}^{M-1} STFT(m,k) = \sum_{m=0}^{M-1} \Psi_k(m) = S(k).$$

In the L-statistics form of this summation we will, for each k, omit $M - M_Q$ of the highest values of $\Psi_k(m)$ and produce the L-estimate of $S(k)$, denoted by $S_L(k)$, as

$$S_L(k) = \sum_{m=0}^{M_Q-1} \Psi_k(m) \tag{11}$$

where $M_Q =$int$[M(1 - Q/100)]$ and Q is the percent of omitted values.

To illustrate this procedure, we eliminated 40% of the top amplitude values of the STFT from the previous example. In this way, we completely eliminated the m-D component from the TF representation. We are left with 60% of the low amplitude values of the STFT, that contain only the rigid body. The FT reconstruction is performed based on these values only. The reconstructed FTs for the cases of a weak and a strong m-D are shown in Figure 9(d,h), respectively. The FT of the rigid body is in both cases successfully reconstructed by summing 60% of the sorted STFT samples, remained after m-D separation. Note that the result is not significantly influenced by the value of σ_R, since the points corresponding to the m-D signature are removed, meaning that their values are almost not important.

In the data analysis, this approach, based on elimination of a part of data, before analyzing the rest of the data, is known as the L-statistics [51].

Analysis of the Missing Values

Since we have eliminated some of the TF representation (TFR) values, we will analyze the influence of incomplete sum in (8). This is the same theory like the L-statistics theory applied to the noisy or non-noisy data, [51].

Assume that only points in $m \in D_k$ are used in summation:

$$S_L(k) = \sum_{m \in D_k} STFT(m,k), \tag{12}$$

where, for each k, D_k is a subset of $\{0, 1, 2, ..., M-1\}$ with M_Q elements.

Within the framework of the previous analysis, it means that there will be a highly concentrated component $S(k)$ surrounded by several low-concentrated values $\sum_{m \notin D_k} STFT(m,k)$. Note that the amplitude of $STFT(m,k)$ is M times lower than the amplitude $S(k)$, since $S(k)$ is obtained as a sum of M values of the STFT. In general, by removing let say $(M - M_Q)$ values in m, we will get one very highly concentrated pulse, as in $S(k)$, and $(M - M_Q)$ values of low-concentrated components of the type $STFT(m,k)$, being spread around the peak of $S(k)$ and summed up by different random phases. Only the peak value is summed in phase. Consider:

1. Case for $k = k_0$ corresponding to the position of the rigid body point: At this frequency, all terms in the sum (10) are the same and equal to $W(0)$. Thus, the value of $S_L(k)$ does not depend on the positions of the removed samples. Its value is $S_L(k_0) = M_Q W(0)$.

2. Case for $k = l + k_0$, where $l \neq 0$: Removed terms in (10) are of the form $\mathbf{x}_l(m) = W(l)e^{j2\pi ml/M}$. They assume values from the set $\Phi_l = \{W(l)e^{j2\pi ml/M},\ m = 0, 1, 2, ..., M-1\}$, with equal probability, for a given l. The statistical mean of these values is $E\{\mathbf{x}_l(m)\} = 0$ for $l \neq 0$, resulting in $E\{S_L(l + k_0)\} = 0$.

The resulting statistical mean for any k is

$$E\{S_L(k)\} = M_Q W(0)\delta(k - k_0).$$

The higher order statistical analysis of this process could be performed in detail, but it is out of the scope of this report. Here, the influence of the number of missing points to the concentration of the reconstructed FT will be illustrated by an example, Figure 10. Here we consider a constant frequency signal, without m-D. Its FT is calculated and presented in Figure 10(a). Then the FT is reconstructed based on $25\%, 50\%$ and 75% of the low amplitude values of the STFT for each k. We can see that even by taking a small number of STFT points, we still keep a strong peak, since it is summed in phase, Figure 10(b),(c),(d).

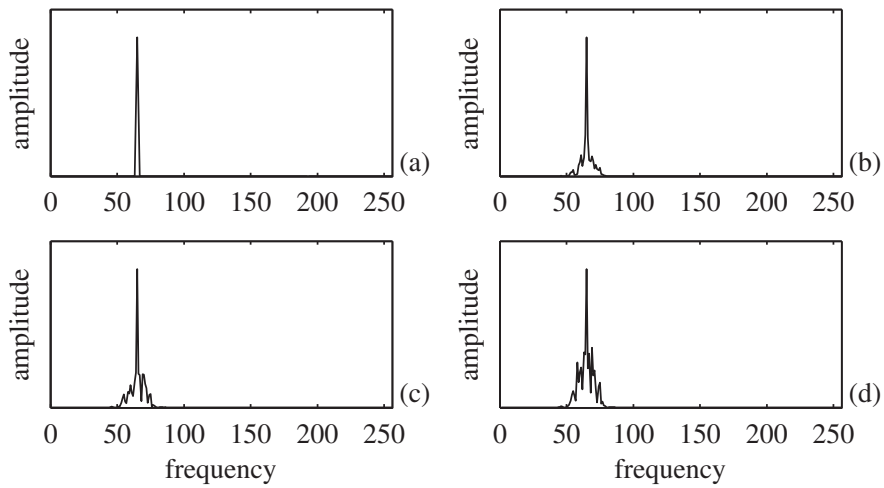

Figure 10: *The FT of a sinusoidal signal: (a) Original, (b) Reconstructed by summing 75% of the smallest STFT values, for each k, (c) Reconstructed by summing 50% of the smallest STFT values, (d) Reconstructed by summing 25% of the smallest STFT values.*

Noise Influence

It is well known [51] that the L-statistics is a tool for robust time-frequency analysis. The robustness comes from the fact that the L-statistics based calculation avoids highest values, which are the most influenced by noise. Therefore, we may expect that by using the L-statistics we will not degrade the radar imaging performance in the case of noise. By using the L-statistics we will eliminate a part of the signal, that is summed in phase in the FT, but we will also eliminate the signal values that are mostly corrupted by noise. Thus, with the elimination of the m-D we will improve the overall performance in the noisy signal cases, as well. In the case of impulse noise, we may expect significant improvement, even in the case without m-D, with a pure rigid body. The effect of noise is statistically analyzed within the simulation study of this report.

High-Resolution Property

Consider the L-statistics application on two very close rigid body points:

$$s(t) = e^{-j2(y_{Bi}-\Delta y_{Bi})\omega_B t\omega_0/c} + e^{-j2(y_{Bi}+\Delta y_{Bi})\omega_B t\omega_0/c}$$

with a very small Δy_{Bi} so that in the FT of the signal $S(\Omega)$, calculated over the entire CIT, we can not distinguish these components. Since the resolution in the Doppler direction is $R_{Dopp} = 2\pi/T_c$ it means $2\Delta y_{Bi} \sim 2\pi/T_c$.

It is surprising, but if we use low concentrated STFT and the proposed L-statistics, we will be able to separate these components. The STFT of these components is

$$STFT(t,\Omega) = \\ W(\Omega + (y_{Bi} - \Delta y_{Bi}))e^{-j\Omega t}e^{-j(y_{Bi}-\Delta y_{Bi})t} \\ +W(\Omega + (y_{Bi} + \Delta y_{Bi}))e^{-j\Omega t}e^{-j(y_{Bi}+\Delta y_{Bi})t}$$

with normalized frequency Ω for $2\omega_0\omega_B/c = 1$.

Note that the STFTs of the components are phase shifted for $\Delta\varphi(t) = 2\Delta y_{Bi}t$. Even for small $2\Delta y_{Bi} \sim 2\pi/T_c$ the phase shift changes are of the order $\Delta\varphi(t) \sim 2\pi/T_c \times T_c$. It means that it could easily change, during the CIT, between 0 and π or even more. Then, there will be time instants in $|STFT(t,\Omega)|$ when the individual STFTs are summed in phase, i.e.,
when $|STFT(t,\Omega)| \cong |W(\Omega + (y_{Bi} - \Delta y_{Bi})) + W(\Omega + (y_{Bi} + \Delta y_{Bi}))|$. Then the signal components can not be separated. However, there will be also the instants in the STFT when the components are with opposite phase,
$|STFT(t,\Omega)| \cong |W(\Omega + (y_{Bi} - \Delta y_{Bi})) - W(\Omega + (y_{Bi} + \Delta y_{Bi}))|$, so that the signal components are clearly separated. We can see that in the first case the values of $|STFT(t,\Omega)|$ will be higher than in the other case. By using the L-statistics approach the higher values will be eliminated, while the lower values, that are well separated, will remain. Thus, we may achieve high signal resolution by using the low concentrated STFT and the L-statistics, even in the case when the separation is not possible in the original FT over the whole CIT.

3.1.3 Adaptive percentage of missing values

There are two possible approaches to establish the threshold for the elimination of the m-D:

The first approach is to assume a fixed threshold for the entire ISAR/SAR image: for example, removing $Q[\%]$ highest values for each frequency, by knowing that this will not disturb significantly the obtained image.

A more sophisticated approach is to calculate the adaptive threshold for each range. The adaptive threshold can be obtained based on the L-statistics. To use the L-statistics approach, we will sort the STFT values for a given range and a given frequency. If there is a m-D, then, after sorting the STFT values, there is a region of an increase of the sorted STFT values, Figure 11 (upper part). Thus, if we sum the sorted STFT values over frequency, we will get a function:

$$A(m) = \sum_k |\Psi_k(m)|^2 . \tag{13}$$

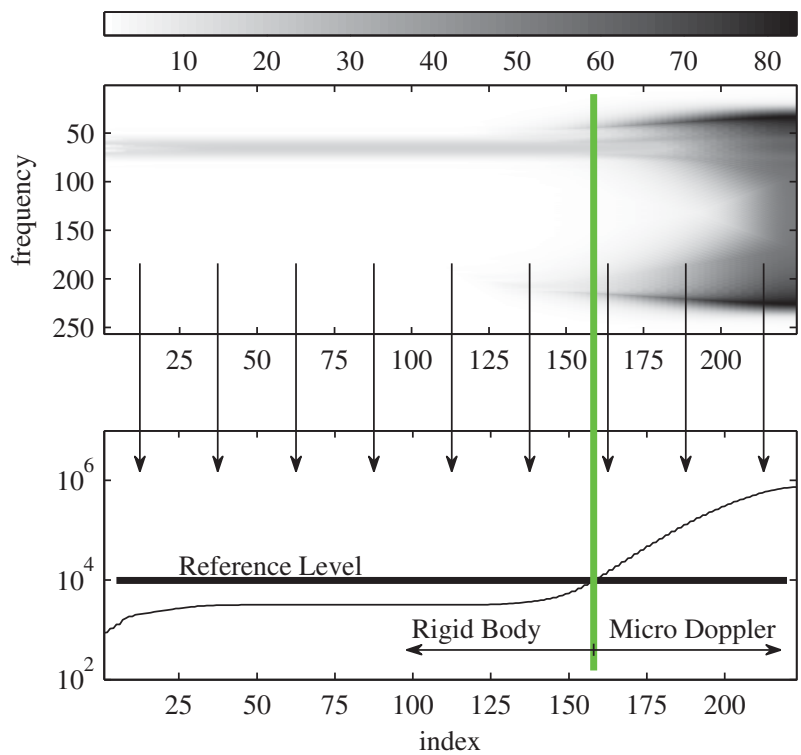

Figure 11: *Sorted STFT values, $|\Psi_k(m)|$, with a colorbar (upper). The values of $A(m)$, obtained by summing the squared values of the sorted STFT along the frequency, with the adaptive threshold R_L obtained based on the average value of 10% of its smallest values - thick horizontal line (lower).*

Now, we can find the reference level R_L based on the mean of 10% of the low amplitude samples, i.e., based on $M/10$ values of the sorted $\Psi_k(m)$, $R_L = T_{hr} \sum_{m=0}^{M/10-1} 10A(m)/M$, with T_{hr} being a parameter, usually from $T_{hr} = 2$ to $T_{hr} = 10$. For example, $T_{hr} = 2$ means that we will use all the values in the sorted $\Psi_k(m)$ whose squared values are up to, for example, 2 times greater than the mean of 10% lowest squared values. Then Q is found as the percent of $A(m)$ below R_L. In the case when there is no m-D it means that we will use all the values, since the stationary values are close to the mean of the lowest values for all time instants. If there is a m-D then the value outside of the stationary points will start to increase sharply and the summation will stop. The results are not too sensitive to these values, since $A(m)$ is a fast increasing function when the m-D starts to appear, Figure 11 (lower part).

In our previous work [5], we have used the L-order statistics. In all phases of the applications, we have used various order statistics of the absolute values of the STFT with various window widths. Here, we use only one window function for the analysis. Then, after sorting the absolute STFT values and defining the threshold Q (by simply assuming, for example $Q = 50\%$, or calculating an adaptive threshold), we return back to perform all the calculations in the complex STFT domain. In this way, we obtain a very simple and efficient model for the calculation, while the results are improved with respect to those obtained by the procedure proposed in our previous work.

3.1.4 Algorithm for the micro-Doppler effects removal

The simplest way to use the proposed method is in applying the L-statistics approach to all range bins, with a constant threshold, for example $Q = 50\%$. In this case the m-D will be separated, while the rigid body will not be degraded. In the case of impulse noise we will benefit from this procedure in each bin. Also, if there are close rigid body components, then this approach will help to resolve them, as it is described earlier. However, this way of calculation increases the calculation complexity.

In radar data analysis, only a part of the range bins may contain the m-D, while most of them will be m-D free. We can improve the calculation complexity by defining a procedure to avoid processing of the range bins where we can conclude that there is no target return or there is no m-D part of signal. If there is an m-D point, then a constant or adaptive threshold for the L-statistics application in the m-D removal could be used in order to separate the m-D, while most of the rigid body part of signal is preserved. If there is no m-D in the considered range bin, then processing for this range is not necessary. If the FT is already well focused, or if there is no returned target signal in the considered range bin, then the FT can be used as it is. Of course, this classification procedure is optional, and we will not lose anything in the radar image quality if we apply the presented method in some bins with already focussed image or where there is no target return. Thus, the thresholds in the next

procedure may be chosen in quite a conservative way, to be sure not to miss any bin with m-D, allowing false m-D detections.

The range bins classification procedure will be presented as an algorithm.

The algorithm consists of the following steps:

Step 1: *Detect whether there is a returned target signal in the considered range bin, by using*

$$\max\{|S(k)|\} > \varepsilon, \tag{14}$$

where $\varepsilon = 0.02 \max\{|S(k,l)|\}$ in the noiseless case or
$\varepsilon = \max\{0.02 \max\{|S(k,l)|\}, 2\sqrt{\sigma}/M\}$ in the presence of noise (here $S(k,l)$ is the 2D FT of the received signal, i.e., full radar image matrix for all ranges and cross-ranges, while $S(k)$ is the radar image for a given range bin). The standard deviation σ of noise in the radar image, for a given range bin, can be estimated as [53]:

$$\hat{\sigma}_{re} = \frac{\text{median}\{|\text{Re}\{S(k)\} - \text{Re}\{S(k-1)\}|\,,\, k = 2,..,M\}}{0.6745\sqrt{2}}, \tag{15}$$

for the real part of $S(k)$. The same applies for the imaginary part. If there is no target in the returned signal, do not perform the following steps and take $S(k)$ as the radar image for the considered range bin. If there is a target signal, continue.

Step 2: *Detect whether there are any m-D effects in the considered range bin:*

$$R = \frac{\max\{|S(k)|\}}{\text{mean}\{|S(k)|\}} > 10.$$

The previous relation is the simplest concentration measure. In the case of a highly concentrated signal, R is close to M, while for a low concentrated signal, this value is close to 1. We say that the signal is well concentrated (rigid body only) if $R > 10$. This threshold was successfully tested for various scenarios and multi-component signals. If the signal is well concentrated take its FT $S(k)$ as the radar image for the considered range bin. If the signal is not well concentrated, continue.

Step 3: *Remove the m-D effects and reconstruct the FT of the reflectors that correspond to the rigid body in the considered range bin.* Remove the values of the STFT that are higher than the threshold and for each frequency sum the rest along the time. Take the obtained FT $S_L(k)$ (12) as the radar image for the considered range bin.

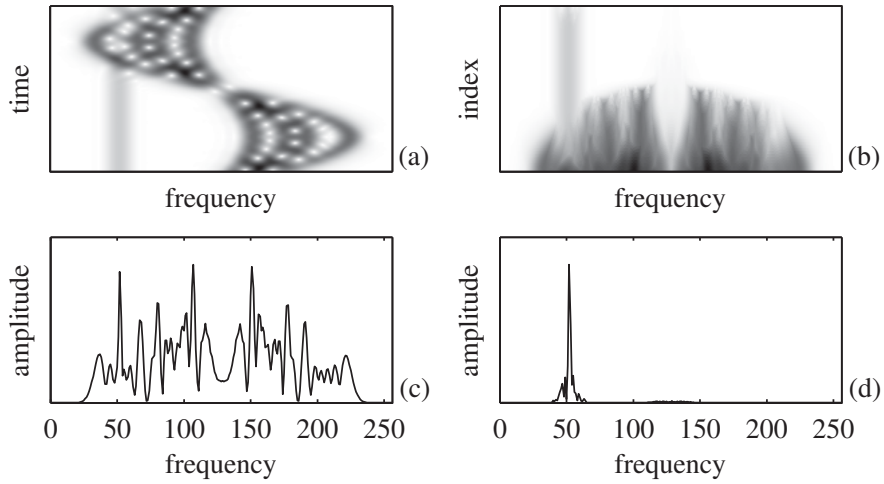

Figure 12: *(a) The STFT of a signal consisting of one rigid body component and four sinusoidally modulated components. (b) The sorted STFT of the same signal. (c) The original FT of the signal. (d) The FT of rigid body, reconstructed by summing the STFT values remaining after sorting and eliminating samples that correspond to the m-D effect.*

3.2 Results

Example 1: The proposed method is tested on a signal with one rigid body point and four sinusoidally modulated components (used to model rotating reflectors),

$$s(m) = \sigma_B \sum_{i=1}^{K} \exp\{jy_{Bi}m\} \tag{16}$$

$$+\sigma_R \sum_{i=1}^{P} \exp\{j[y_{R0i}m + A_{Ri}\sin(\omega_{Ri}m + \varphi_i)]\},$$

with $K = 1$, $P = 4$, $\sigma_B = 1$, $\sigma_R = 3$, $y_{B1} = 0.4\pi$, $A_{Ri} = [96, 48, 64, 24]$, $\omega_{Ri} = \pi/128$, $y_{R0i} = \pi$ and $\varphi_i = 0$, for $i = 1, 2, 3, 4$. The STFT of this signal is presented in Figure 12(a). The m-D, although moderate, significantly covers the rigid body, i.e., the part of the constant frequency component is almost invisible in the sinusoidal patterns. The sorted STFT is shown in Figure 12(b). Then, the highest STFT values are removed, for each frequency in the reconstruction phase. A constant threshold, with $Q = 60\%$ is used here. The FT reconstructed from the remaining STFT samples is shown in Figure 12(d). The rigid body is successfully reconstructed in the presence of the m-D. The original FT of the analyzed signal is given in Figure 12(c).

Example 2: Here, we analyze a signal with 10 components: $K = 5$ components with constant frequency (used to model rigid body reflectors) and $P = 5$ sinusoidally

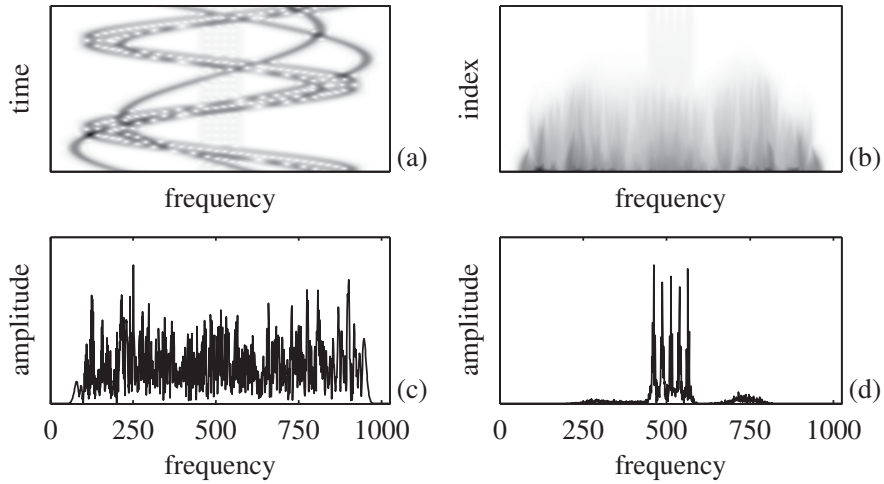

Figure 13: *(a) The STFT of a signal consisting of five rigid body components and five sinusoidally modulated m-D components (b) The sorted STFT of the same signal. (c) The original FT of the signal. (d) The FT of rigid body, reconstructed by summing the STFT values remaining after sorting and eliminating samples that correspond to the m-D effect.*

modulated components (used to model rotating reflectors), (16) with: $\sigma_B = 1$, $\sigma_R = 15$, $y_{Bi} = [1.9\pi, 1.95\pi, 2\pi, 2.05\pi, 2.1\pi]$, $A_{Ri} = [150, 300, 200, 440, 200]$, $\omega_{Ri} = [\pi/256, \pi/512, \pi/256, \pi/512, \pi/256]$, $y_{R0i} = 0$ and $\varphi_i = [0, -\pi/3, \pi/6, -2\pi/3, 0]$, for $i = 1, 2, 3, 4, 5$, $M = 1024$ and $M_w = 64$. The STFT of this signal is shown in Figure 13(a). The constant components, that correspond to the rigid body, are not well separated in the TF plane. Moreover, they are covered by the sinusoidally modulated patterns which represent the m-D effects of the rotating reflectors. If we sort the STFT values along time axis, then the representation of the rigid body parts does not change, since it is constant during the whole CIT, Figure 13(b). On the other hand, the fast rotating parts occupy only a small time intervals over a wide region of frequencies. They lie in high value regions of the sorted transform. Thus, they will be eliminated by removing the highest STFT values, for each frequency. An adaptive threshold, with $T_{hr} = 5$ is used here. The results are not sensitive to the value of T_{hr}. The reconstructed FT, obtained by summing the rest of the STFT (12) along the time is shown in Figure 13(d). We can clearly see five peaks that correspond to the five rigid body reflectors. The original FT is shown in Figure 13(c). It cannot be used even to determine the number of components in the analyzed signal.

Helicopter Data Analysis

Example 3: In this example, we first present a new simulation approach to the data of a German Air Force Bell UH-1D Helicopter known also as 'Iroquois' presented in [5].

Here, the simulation is performed according to the variable flashing reflection coefficients, rather than just by using a mathematical form that would produce the data as in [6]. Several effects are emphasized in the TFR Figure 14(a). The stationary patterns along the time-axis correspond to the rigid body reflection. The motion of two main blades is modeled by two rotating reflectors, producing sinusoidal FM signals with a large magnitude in the frequency direction, (18). The main rotor flashes are simulated by signals producing lines that connects extreme points of the sinusoidal FM signal, along the time axis. The smaller pulses that can be seen on the right-hand side of Figure 14(a) correspond to the tail rotor flashes, and they are simulated here by taking into account the physical meaning of its appearance. Namely, these flashes correspond to the periodic alignment of the main and tail rotors to maximally reflect the radar signal when they are normal to the line-of-sight. Therefore, we use here an angle dependent reflection coefficient

$$\sigma(t) = \exp(-30\,|\sin(2\pi t/T_{Rot})|), \tag{17}$$

where the reflection takes value 1 when $t = kT_{Rot}/2$ and $|\sin(2\pi t/T_{Rot})| = 0$, while for other t, $30\,|\sin(2\pi t/T_{Rot})|$ assumes high values and the reflection coefficient is small. Note that other effects that can be observed in a radar image, including multi-path, are not considered here.

The simplified model of the reflected UH-1D signal can now be written as

$$s(t) = x_{RIG}(t) + x_{ROT}(t) + x_{FL_M}(t) + x_{FL_T}(t),$$

where $x_{RIG}(t)$, $x_{ROT}(t)$, $x_{FL_M}(t)$ and $x_{FL_T}(t)$ represent signals caused by the rigid body, rotation of the main rotor, and the main and tail rotor flashes, respectively. The signal is considered within the interval of 400 ms, sampled with a rate of $\Delta t = 1/48$ ms. Four sinusoidal components, caused by the rigid body, are at the frequencies -10.3 kHz, -2.5 kHz, 2.3 kHz and 2.7 kHz. Two components at -0.4 kHz and 0.4 kHz correspond to the modulated time tones commonly added to the data tape [56]. The sinusoidal FM signals, corresponding to the rotation of the main rotor blades, are modeled as

$$\begin{aligned} x_{ROT}(t) = \sigma_{ROT}[&e^{j2\pi A_{ROT}\sin(2\pi t/T_{ROT})} \\ &+e^{-j2\pi A_{ROT}\sin(2\pi t/T_{ROT})}], \end{aligned} \tag{18}$$

where $\sigma_{ROT} = 10$, $T_{ROT} = 175$ ms and $A_{ROT} = 529.19$. The main and tail rotor flashes are modeled as

$$\begin{aligned} x_{FL_M}(t) = 2.5 \sum_{k=1}^{128} \frac{k+64}{128} e^{-30|\sin(2\pi t/175)|} \\ \times \cos(25.98k \sin(\frac{2\pi t}{175})), \end{aligned}$$

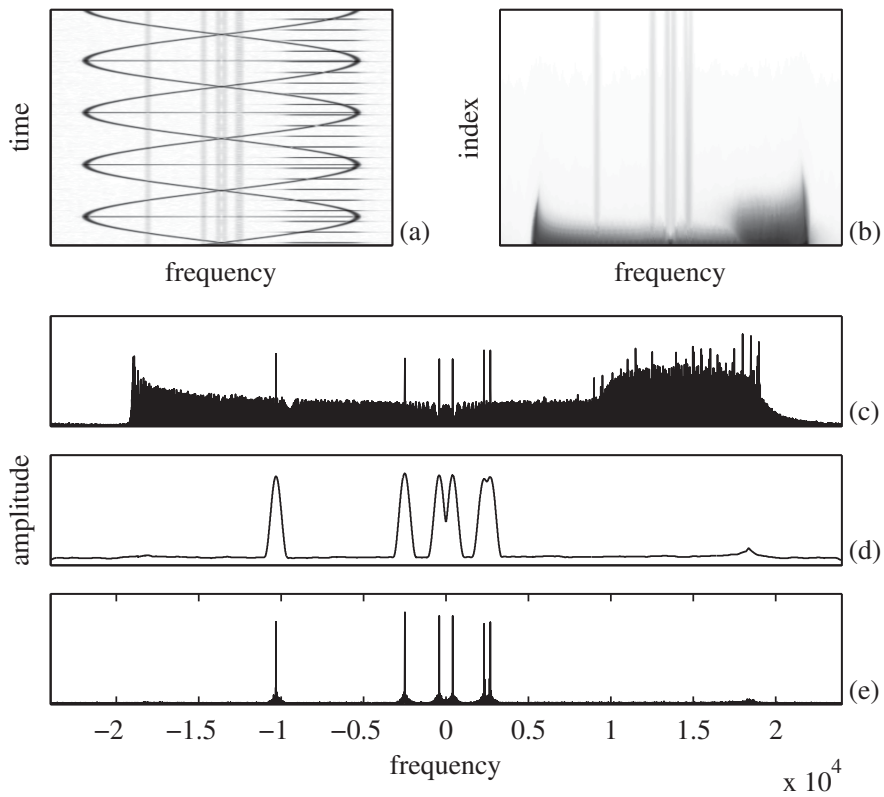

Figure 14: *(a) The STFT of a simulated signal of a German Air Force Bell UH-1D Helicopter. (b) The sorted STFT of this signal. (c) Original FT of the signal. (d) The FT of the rigid body, reconstructed by summing the lowest absolute STFT values. (e) The FT of the rigid body, reconstructed by the proposed method.*

and

$$x_{FL_T}(t) = 2.5 \sum_{k=64}^{128} e^{-30|\sin(2\pi t/35.8)|} e^{(j(2.66k \sin(4\pi t/35.8)))}.$$

The signal is corrupted by a moderate Gaussian noise. To compare our simulation with the real one (for the m-D and rigid part values ratio) refer to [6, 56].

The proposed algorithm for the rigid body separation is applied to the simulated helicopter signal. The sorted STFT is shown in Figure 14(b). We can see that the STFT values corresponding to the rotating parts are in the high value region. The reconstructed FT is shown in Figure 14(e). All 5 reflectors that correspond to the rigid body are successfully recovered. The original FT is presented in Figure 14(c), while the reconstructed FT obtained by summing the absolute values of the remaining STFT samples is presented in Figure 14(d).

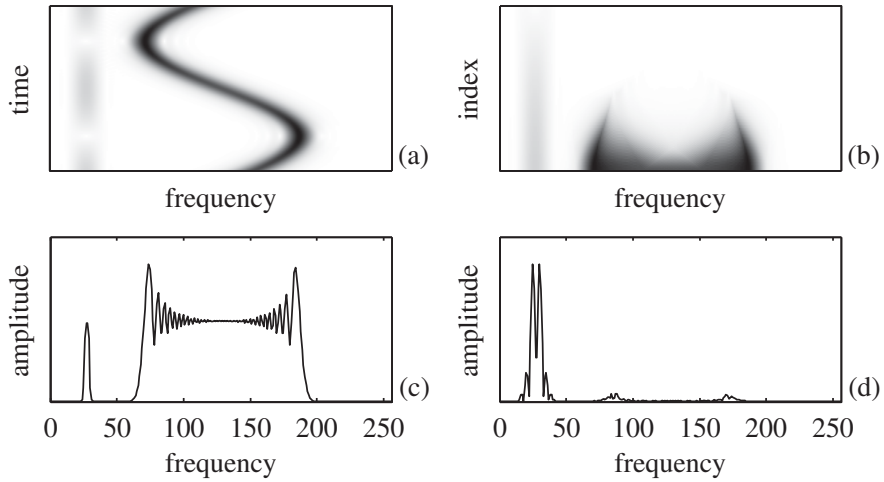

Figure 15: *(a) The STFT of a signal consisting of two very close components with constant frequency and one sinusoidally modulated component. (b) The sorted STFT of the same signal. (c) The original FT of the signal. (d) The FT of rigid body, reconstructed by summing the lowest STFT values.*

High-Resolution Analysis

Example 4: Two very close rigid body reflectors in the presence of m-D effects are simulated in this example

$$s(m) = e^{-j201\pi m/M} + e^{-j205\pi m/M} + 10e^{j58\cos(2\pi m/M)},$$

where $M = 256$ samples are used. The window with $M_w = 32$ zero-padded to M is used for the STFT calculation. The STFT of the analyzed signal is presented on Figure 15(a), while the sorted STFT is presented on Figure 15(b). It can be seen in Figure 15(a), that there are time instants when the STFTs of the close components are summed with opposite phase, and they appear as separated. On the other hand, when the close components are summed in phase, they are not separated. Moreover, as it can be seen from the sorted STFT, presented in Figure 15(b), when the STFTs are summed in phase, the resulting STFT is higher. Consequently, by removing the highest values of the STFT, the remaining lower values are well separated; thus, the close components are separated. The FT reconstructed by summing over time 50% of lowest samples of the STFT, is shown in Figure 15(d), while the original FT is shown in Figure 15(c). We can see that the separation of the close components is achieved by the proposed method, although it is not possible in the original FT (the distance between two maxima positions is biased).

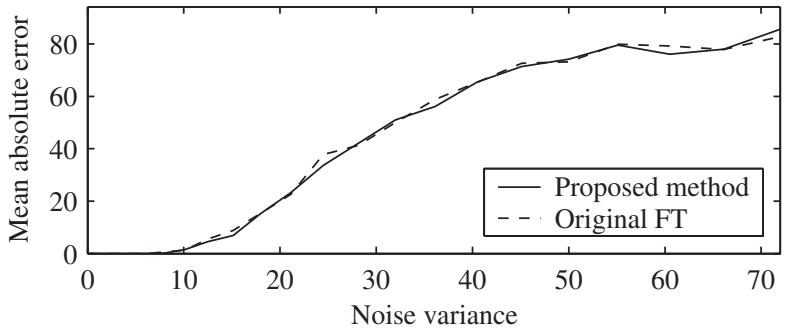

Figure 16: *Mean absolute error as a function of noise variance calculated for the case of one rigid body reflector without m-D. The solid line corresponds to the proposed method, while the dashed line corresponds to the full FT.*

Noise Influence Analysis

Example 5: One stationary reflector and one m-D reflector are considered. Complex valued, white Gaussian noise $\varepsilon(t)$, with variance σ_ε^2, is added

$$s(m) = e^{-j0.75\pi m} + \sigma_R e^{j58\cos(2\pi m/256)} + \varepsilon(t),$$

where σ_R is the reflection coefficient of the m-D reflector. The noise variance is varied within a wide range $0 \leq \sigma_\varepsilon^2 \leq 72$ (from the case without noise up to the case when noise dominates), with step 1. For each variance value from this range, 1000 Monte Carlo simulations are performed. In each realization, we have found a position of the maximum in the L-statistics based estimate of the FT, $S_L(k)$. Then, the error is calculated as a difference of this position and the true signal frequency. The mean absolute error is calculated for each variance for 1000 realizations and the mean absolute error is plotted for various noise variance values. For the rigid body FT reconstruction we used, for each frequency, 50% of the smallest STFT values in the L-statistics summation.

We start with the case of pure stationary point $\sigma_R = 0$, to see how the L-statistics approach, with 50% of values, influences the results. It is well known that the FT transform is theoretically the best (ML) estimator for a pure sinusoid in Gaussian noise. The corresponding mean absolute error is depicted in Figure 16. The solid line corresponds to the proposed method, while the dashed line corresponds to the full FT. The FT is well reconstructed with the proposed L-statistics based method and the estimation results are not degraded with respect to the full FT, in this simple case, when the FT is the ML estimator.

We have analyzed noise influences in the case of $\sigma_R = 5$, as well. For the noiseless case, the STFT is shown in Figure 17(a), while the sorted STFT is shown in Figure 17(b).

The original FT is presented in Figure 17(c). The FT reconstructed by summing, for each frequency, 50% of the lowest STFT samples is shown in Figure 17(d). The same plots for the case of $\sigma_\varepsilon^2 = 4.5$, $SNR = -6.53\,\text{dB}$ are shown in Figure 17(e–h). The signal to noise ratio (SNR) is calculated as the rigid body part of the signal to the noise ratio, in all cases. We can see that the proposed method successfully reconstructs the FT of the rigid body in the presence of m-D and noise.

The mean absolute error of the proposed method and the original FT is shown in Figure 17(i). The proposed method does not only reconstruct the FT successfully, but also eliminates the m-D effect and outperforms the original FT, whose estimation performance is degraded by the m-D effect.

Example 6: We analyzed one more case of one stationary reflector and one m-D reflector in the presence of noise. Here, the m-D reflector is stronger and closer to the stationary one. The corresponding signal is of the same form as in the previous example, but with $\sigma_R = 10$, while the rigid body reflector signal component is at the frequency $f_B = 0.125\,\text{Hz}$. The same statistical analysis and reconstruction procedure as in the previous example are performed.

For the noiseless case, the STFT is shown in Figure 18(a), while the sorted STFT is shown in Figure 18(b). The original FT is presented in Figure 18(c). The FT reconstructed by summing, for each frequency, 50% of the lowest STFT samples is shown in Figure 18(d). The same plots for the case of $\sigma_\varepsilon^2 = 4.5$, $SNR = -6.53\,\text{dB}$ are shown in Figure 18(e–h). We can see from Figure 18(d) and Figure 18(h) that the performance of the proposed method does not degrade even in the case of strong m-D reflector positioned close to the rigid body reflector; in this case, the stationary and m-D components are crossing in the STFT, Figure 18(a) and Figure 18(e). The proposed method continues to successfully reconstruct the FT of the rigid body in the presence of noise, Figure 18(h), while the FT is not even able to indicate that there is a rigid body reflector, at all, Figure 18(g).

The mean absolute error of the proposed method and the original FT are shown in Figure 18(i). From the presented statistics, we can confirm that, even in the presence of noise and close reflectors with strong m-D effects, the proposed method successfully reconstructs the FT of the rigid body, while the original FT completely fails to indicate the rigid body existence.

Non-Compensated Rigid Body Acceleration

Example 7: In this case an accelerating rigid body target is considered and examined. The received radar signal that corresponds to an accelerating target in the ISAR systems is a linear FM signal. Similarly, in SAR systems the target motion may induce linear frequency modulation in the received radar signal [9]. Therefore, we simulated three rigid body reflectors as three linear FM components with the chirp-

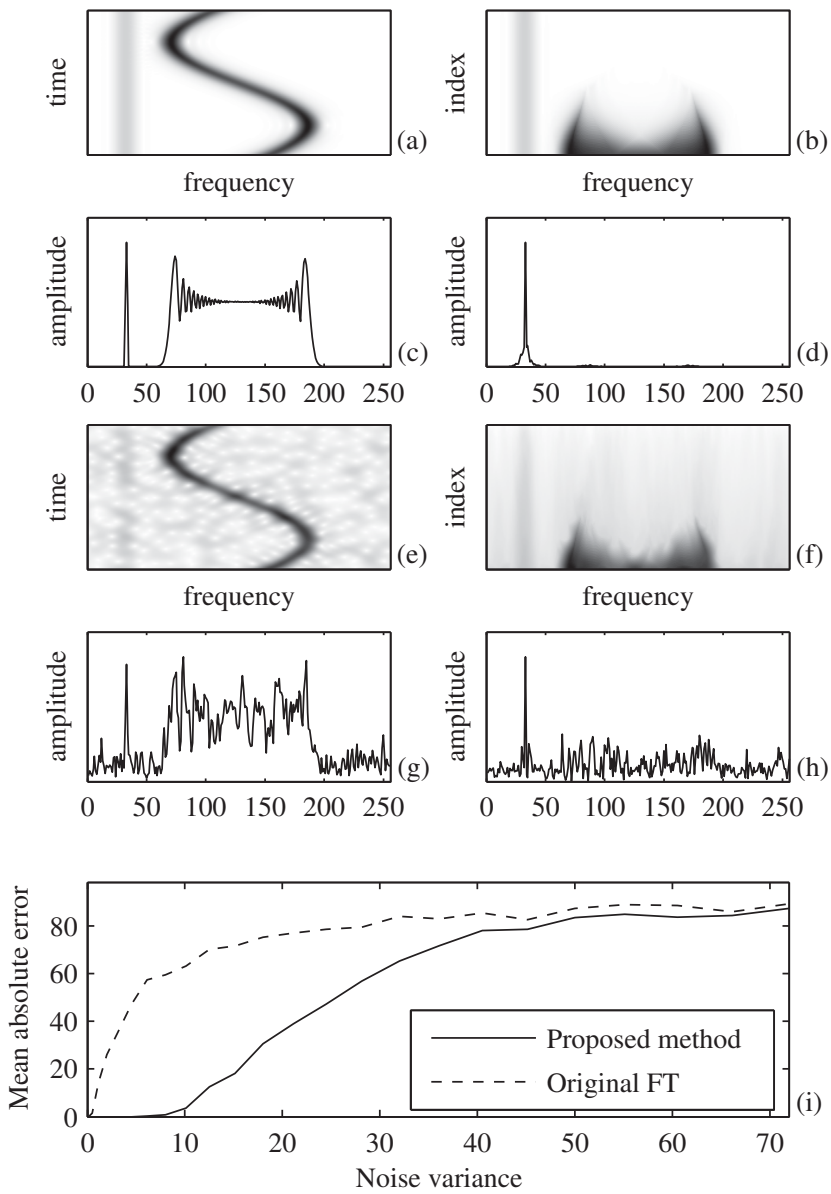

Figure 17: *One rigid body reflector and one m-D reflector. Noiseless case (a–d): (a) The STFT absolute value, (b) Sorted STFT, (c) The original FT, (d) Reconstructed FT. A realization of noisy case with* $\sigma_\varepsilon^2 = 4.5$ *(e–h): (e) The STFT absolute value, (f) Sorted STFT, (g) The original FT, (h) Reconstructed FT. (i) Mean absolute error as a function of noise variance in* 1000 *noisy realizations.*

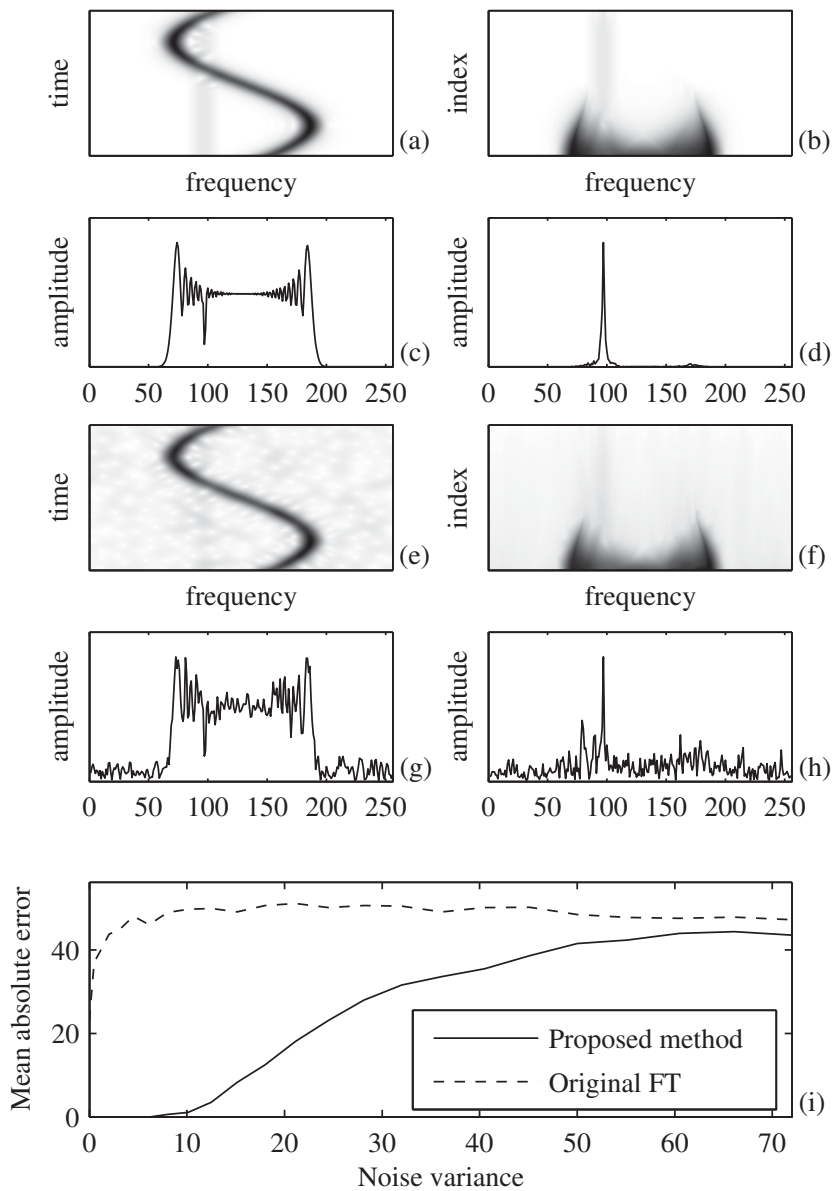

Figure 18: *One rigid body reflector and one close m-D reflector. Noiseless case (a–d): (a) The STFT absolute value, (b) Sorted STFT, (c) The original FT, (d) Reconstructed FT. A realization of noisy case with* $\sigma_\varepsilon^2 = 4.5$ *(e–h): (e) The STFT absolute value, (f) Sorted STFT, (g) The original FT, (h) Reconstructed FT. (i) Mean absolute error, in* 1000 *noisy realizations, as a function of noise variance.*

rate a. In order to show that our algorithm will not remove only the m-D induced by vibrating and rotating targets, here we have also used a more complex form of the m-D. In this example, we will show that the algorithm is robust to the effects of acceleration.

The STFT of the analyzed signal is presented in Figure 19(a). We can clearly see that, as a result of the acceleration, the TFR of the rigid body part of the signal is not stationary during the time. Consequently, it is difficult to separate it from the m-D in the sorted STFT, Figure 19(b). Namely, if we perform the m-D separation by removing 50% of the highest STFT samples, as we did in the examples where there was no need for the motion compensation, we would reconstruct the FT of the rigid body as presented in Figure 19(d). Here, we have removed a significant part of the rigid body points, as well.

In the analysis of the rigid body with uncompensated acceleration, we should first compensate the remaining acceleration. This is not possible in the original signal, since the m-D signatures prevent us from properly compensating the remaining acceleration. However, the application of the proposed method for the m-D removal can solve this problem, as well. We will use the Local Polynomial Fourier Transform (LPFT)

$$LPFT(t,\Omega) = \int_{-\infty}^{\infty} s(\tau)w(\tau - t)e^{-j(\Omega\tau+\alpha\tau^2)}d\tau, \tag{19}$$

instead of the STFT, where the term $exp(-j\alpha\tau^2)$ is used to compensate the linear frequency modulation of the rigid body part of the signal, $LPFT(t,\Omega) = FT\{s(\tau)e\,w(\tau^2 - t)\}$. The parameter α is not known in advance, but we know that it can take values from a set $\Lambda = [-\alpha_{\max}, \alpha_{\max}]$, where $\alpha_{\max}$ is the chirp rate corresponding to the maximal expected acceleration (positive or negative), [57]. In this example we used $\Lambda = [-2 : 0.25 : 2]$. Now, $\hat{\alpha}$ can be estimated as the value from the set Λ for which we obtain the highest concentration of the reconstructed rigid body (compensated FT) based on the LPFT and the L-statistics, with, for example, $Q = 50\%$. The reconstructed FT, by using 50% of the lower LPFT values, will be denoted by $S_{L,\alpha}(k)$. Its concentration is calculated using the time-frequency concentration measure [58],

$$H(\alpha) = \left(\sum_{k=0}^{M-1} |S_{L,\alpha}(k)|^{1/p} \right)^p , \tag{20}$$

with $p = 1$. The LPFT, calculated with the estimated optimal value of $\hat{\alpha} = 1.25$, which results from $H(\alpha)$, is shown in Figure 19(e). The linear frequency modulation is compensated by $\hat{\alpha}$ in (19). Thus, with optimal $\hat{\alpha}$ we have components with almost constant frequency in the TFR representation of the rigid body reflectors. In this way, we have successfully reconstructed the rigid body and removed the m-D part, as it is presented in Figure 19(h). The procedure is not too sensitive to $\hat{\alpha}$. Very good results are obtained with neighboring values $\hat{\alpha} = 1.0$ and $\hat{\alpha} = 1.5$.

Note, that it would be impossible to estimate the chirp-rate $\hat{\alpha}$ from the original signal, without employing the proposed algorithm for the m-D removal.

Real Data Application

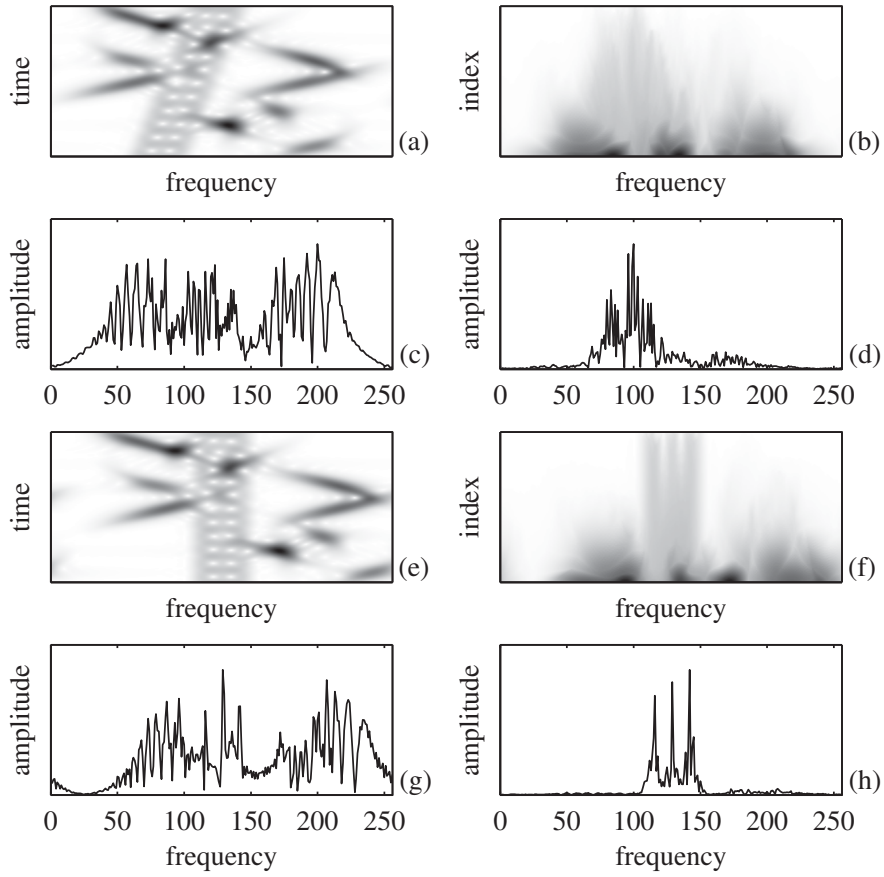

Figure 19: *Accelerating rigid body with a complex form of the mD. (a) TFR of the signal without motion compensation. (b) Sorted TFR of the original signal. (c) Original FT of the analysed signal. (d) Reconstructed FT of the accelerating rigid body without motion compensation. (e) TFR of the signal after motion compensation. (f) Sorted TFR of acceleration compensated signal. (g) The FT of the original signal with motion compensation. (h) Reconstructed FT of the accelerating rigid body with motion compensation.*

Example 8: The proposed algorithm is tested on real data in this example. The examined data were collected using an X-band radar operating at 9.2 GHz, [4]. The first real data represent three corner reflectors rotating at approximately 60 RPM (rotation per minute) and the rigid body observed by the radar with $T_r = 1\,\text{kHz}$. The STFT of the returned signal, for the given range bin, is shown in Figure 20(a).

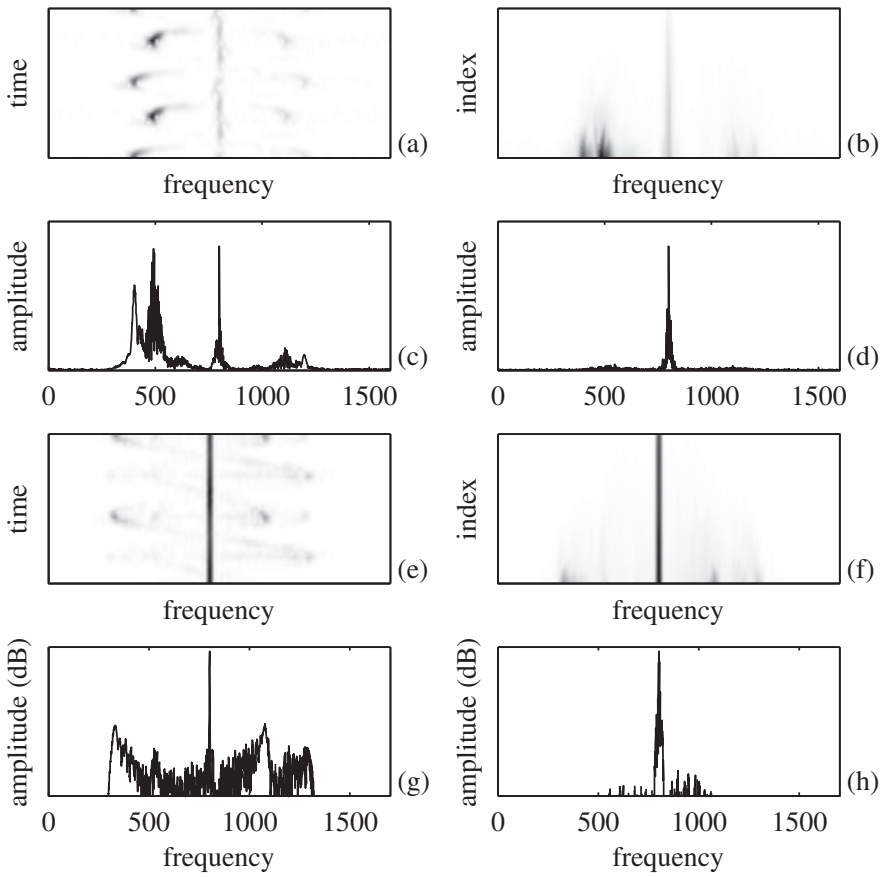

Figure 20: *Real radar data corresponding to a rigid body and three corner reflectors rotating at* ~ 60 *RPM (a–d). (a) the STFT. (b) Sorted STFT. (c) The original FT and (d) the FT reconstructed by summing over* 50% *of the lowest STFT samples. The same procedure is repeated for real radar data corresponding to a stronger rigid body and two corner reflectors rotating at* ~ 40 *RPM (e–h). A logarithmic amplitude scale is used in subplots (g) and (h).*

After sorting the STFT over time Figure 20(b), the constant frequency component corresponding to the rigid body becomes more visible, since the time varying frequency content is spread over many frequencies, for each frequency bin. The rigid body is separated from the m-D and its FT is successfully reconstructed by using 50% of the lowest STFT values, as shown in Figure 20(d). If we compare it to the FT of the original signal, Figure 20(c), we can see the improvement in the rigid body presentation.

In the second example, the real radar data corresponding to two outside corner reflectors, rotating at approximately 40 RPM (all facing radar) with rigid body, are analyzed. The same radar as in the previous example is used, while the reflectivity of rigid body is much higher than those of the rotating reflectors. The STFT representation of the observed signal is shown in Figure 20(e). The sorted STFT is shown in Figure 20(f). The original FT is shown in Figure 20(g). The reconstructed FT, obtained by summing 50% of the lowest STFT values is presented in Figure 20(h). We have successfully removed most of the m-D. Moreover, we may use the removed STFT samples in order to estimate features of rotating reflectors. Here, we have used a logarithmic scale to present the reconstructed values, since the m-D values were very low.

4 Micro-Doppler toolbox

The micro-Doppler toolbox is a set of functions for the analysis of m-D in radar return signals. Two approaches are implemented.

- L-statistics is used in order to separate the m-D and the rigid body from the analysed range bin.
- Micro-Doppler parameter estimation is performed in order to estimate the m-D frequency, amplitude and phase. The parameter estimation method based on the inverse Radon transform is developed. The developed method is capable to detect m-D parameters even in the case of multicomponent m-D signal.
- The toolbox is capable to deal with one-dimensional (1D) and two-dimensional (2D) signals. If the 2D signal is analyzed, a procedure for detection range bins with possible m-D is implemented.
- The toolbox offers link to the Time-Frequency Analysis toolbox in order to provide highly concentrated time-frequency representation of the analyzed signal.

Beside core functions for L-statistics and inverse Radon transform-based parameter estimation, the toolbox contains Virtual Instrument and Demo.

4.1 Files and installation

This toolbox has six program files:

L_statistics.m The function takes single range bin signal (in time domain) and performs separation of rigid-body and m-D parts of the analyzed signal. For more information type `help L_statistics` in command line.

MD_iradon.m This function estimates parameters of m-D component. It is suitable for single-component m-D signals. In multi-component signals, the m-D function estimates parameters for one component only.

MD_iradonMC.m This function estimates parameters of m-D in multi-component case. After the estimation of parameters, the estimated component is removed from the analyzed signal and the estimation procedure is repeated for the next component.

MD_VI.m Virtual Instrument for m-D analysis.

MD_demo.m Demonstration of core functions usage.

STFT_TFR.m Short-time Fourier transform calculation. This function is part of the Time-Frequency Analysis toolbox.

SM_TFR.m S-method calculation. This function is part of the Time-frequency Analysis toolbox.

test_mat_file.mat Matlab file with 1D and 2D data variables. This file is used for testing the External data 1D and External data 2D functionality.

To install the toolbox, copy all files in the working directory. Alternatively, files can be copied in the directory that includes MATLAB path.

4.2 Virtual instrument

- Virtual Instrument is started with command `MD_VI`. The main screen is displayed in Figure 21.

4.2.1 Main screen

- The main screen is divided into three parts. The left part is dedicated to the definition of the input data. The center part deals with L-statistics as a method for separating m-D and rigid body parts of the analyzed signal. The right part is for the m-D parameter estimation.

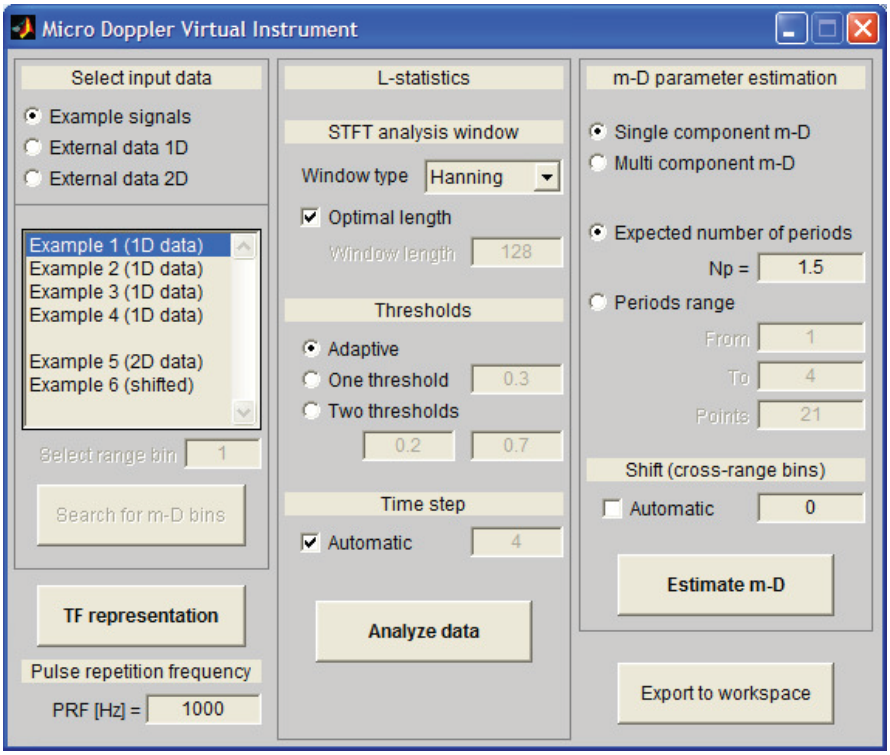

Figure 21: *Virtual Instrument – main screen*

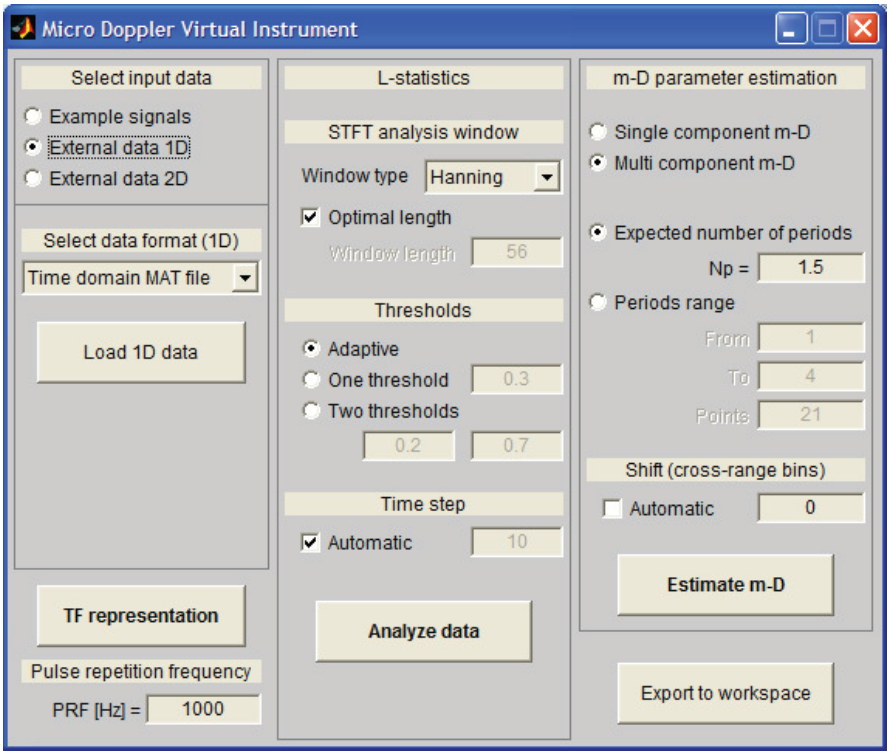

Figure 22: *Load 1D external data*

- The input data can be simulated signals, 1D external data or 2D external data.
- If example signals are selected, the user can choose one of six predefined data sets, where Example signals 1-4 and Example signal 6 are 1D data and Example signal 5 is 2D data.
- When the example signal is selected, the ToolTip with explanation of the chosen signal is displayed if the user hold the mouse over the example list.
- In the 2D data case, the edit box with range-bin selection and the button for search of m-D range bins are enabled.
- When the user select the data, it is allowed to plot TF representation of the selected data.
- The pulse repetition frequency can be defined in the lower part of the left side of the Virtual Instrument.
- If 1D external data is selected, the user can select the data format (time domain or frequency domain) and load the data from external MATLAB file as presented in Figure 22.
- If variable q is detected in the input file, q is used as input data. Otherwise, the user can choose 1D variable from the data file to use it as input data.
- When 2D external data is selected (Figure 23), the user has choices as in the previous case except the user can now transpose the input data if the range bins are not in rows, and the range bin should be selected prior to further analysis.
- In this case, if the variable q is not found in the selected MAT file, the user can select 2D variable that contains radar data.

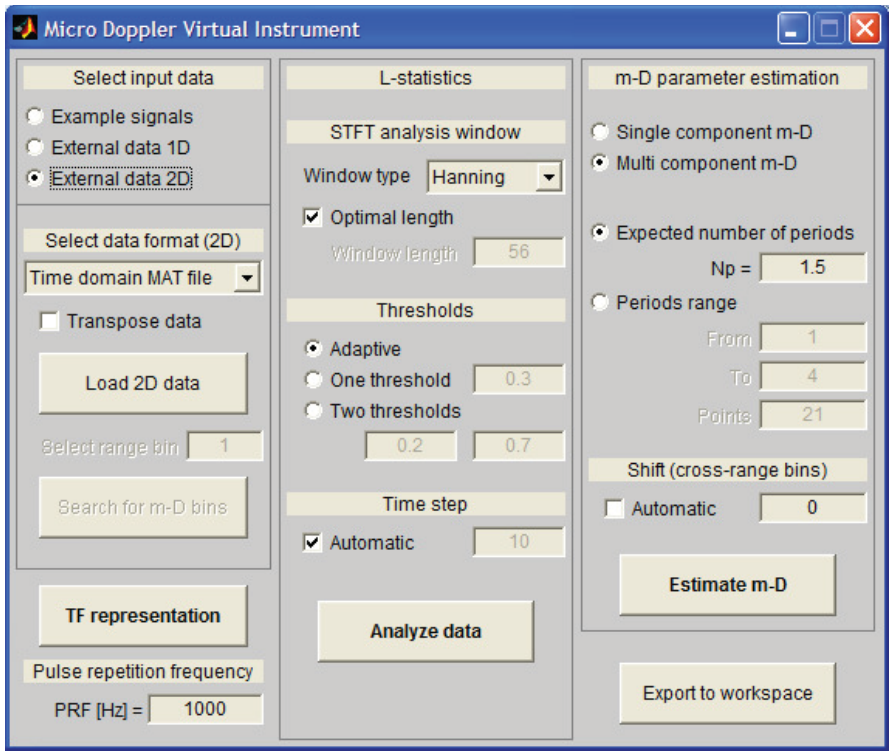

Figure 23: *Load 2D external data*

4.2.2 Time-frequency data representation

- Click on the TF representation button that gives the TF representation of item the selected data. Example 4 is presented in Figure 24. The S-method with $L = 2$ and the appropriate time domain window is used in this example.

4.2.3 L-statistics

- The middle part of the Virtual Instrument screen (Figure 21) is dedicated to L-statistics.
- The user can select the window type and window length (or determine the window length automatically according to concentration measures).
- In the second step, the user can define thresholds for the m-D and rigid body parts separation or can choose adaptive threshold.
- In the third step, the user can define the time-step for the STFT or use automatically determined time-step.

- Click on the Analyze data button provides results in a form similar to Figure 25.
- The upper left subplot is the TFR (time-frequency representation) of the analyzed data. The sorted values of the TFR along with threshold(s) are presented in the upper right subplot.
- The Fourier transform of the original signal and the rigid body part are presented in the lower left two subplots.
- The lower right subplot is the TFR of the m-D part of the analyzed signal.

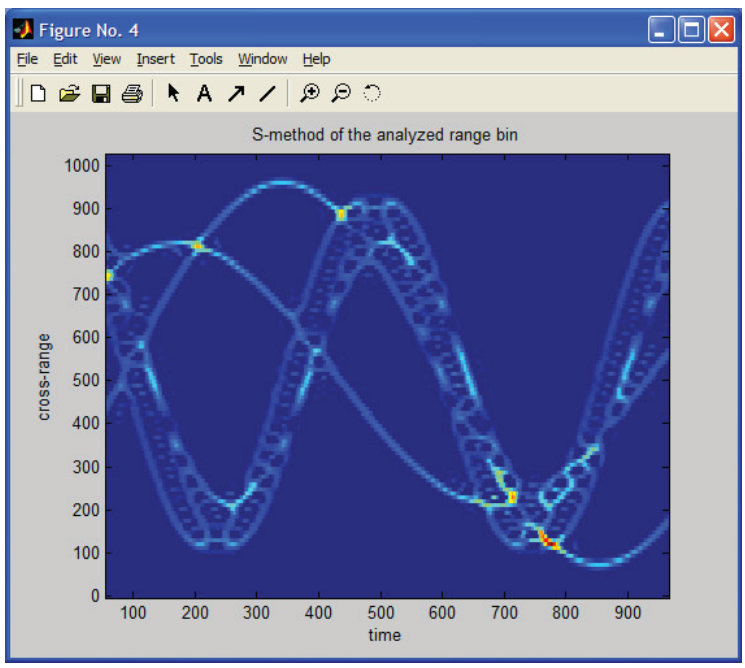

Figure 24: *Time-frequency representation of the analyzed data*

4.2.4 Micro-Doppler parameter estimation

- The third part of the Virtual Instrument is dedicated to the m-D parameter estimation based on the inverse Radon transform.
- The user can select between the single or multi component case.
- Furthermore, the user can give expected number of periods within the analyzed image or define the period range.
- In cases when the m-D signal is not centered around the middle cross-range bin, the user can define the cross-range shift or chose the shift automatically.

- Click on the Estimate m-D button when single component m-D is selected; this gives results as illustrated in Figure 26 and Figure 27.
- Figure 25 presents the TF representation of the analyzed data along with estimated m-D (black line).
- Estimated m-D parameters (Rate, Amplitude, Phase and the number of periods) are given in the message-box presented in Figure 27.

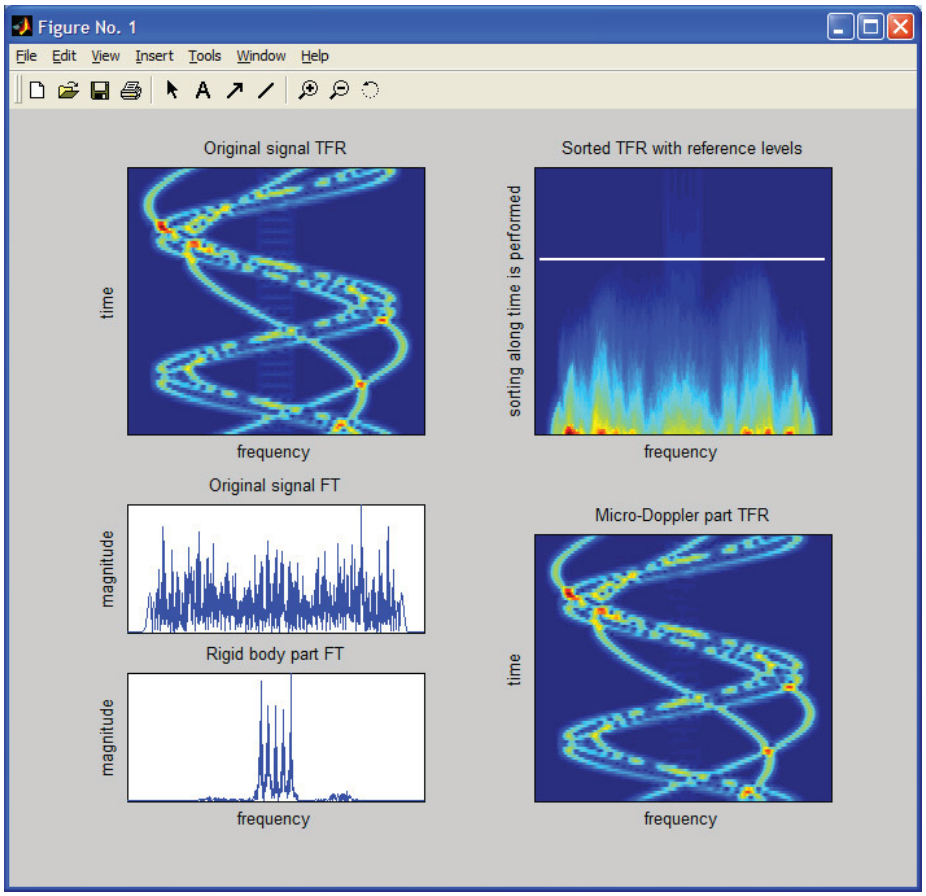

Figure 25: *L-statistics analysis*

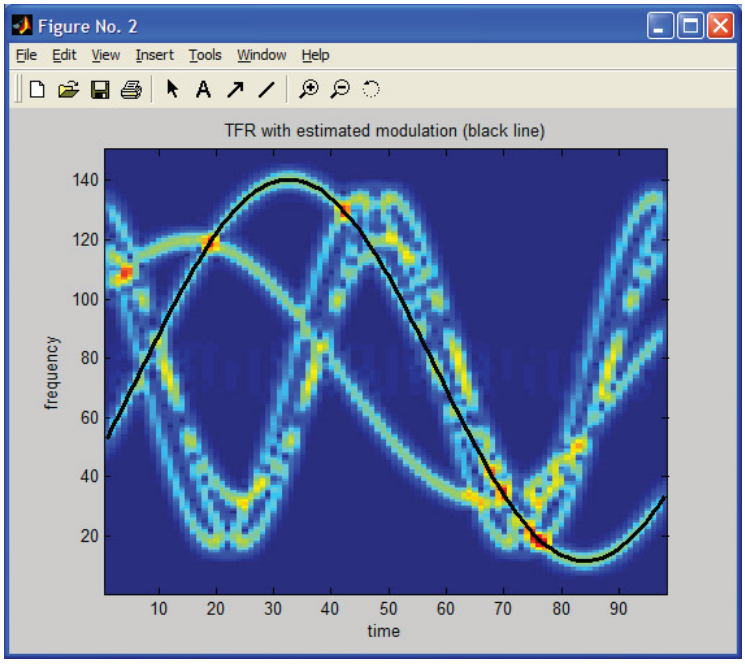

Figure 26: *Micro-Doppler parameter estimation results*

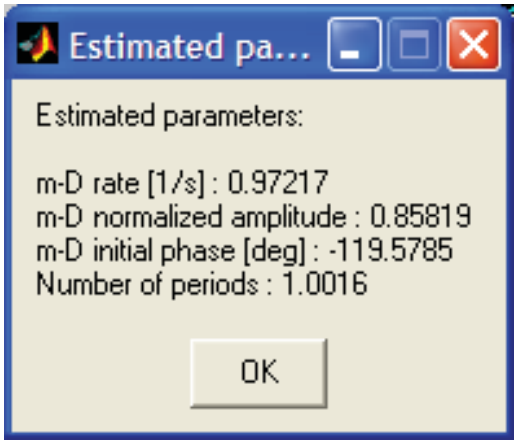

Figure 27: *Micro-Doppler parameters*

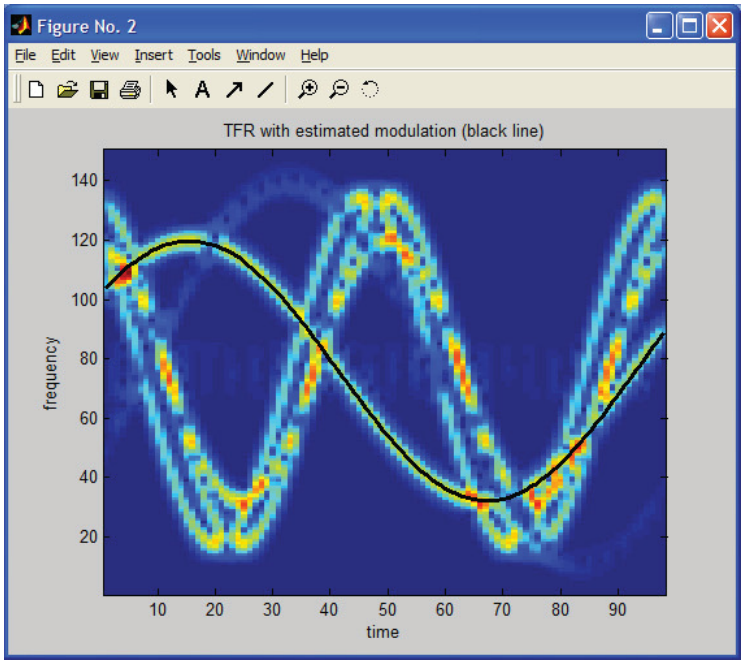

Figure 28: *Micro-Doppler parameter estimation results – multicomponent case – second analyzed component*

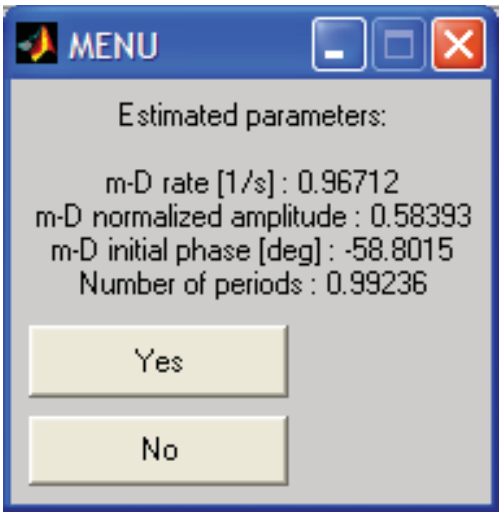

Figure 29: *Micro-Doppler parameters for second component in multi-component case*

When the multicomponent m-D is selected, the search procedure is repeated in order to detect all m-D components. Results are presented in Figure 28 for the second component in the analyzed signal. Parameters of the analyzed component are displayed and the user can choose to search for another component or to stop analysis (Figure 29).

4.2.5 2D data analysis

- If 2D data is analyzed, the user can activate the search for m-D bins resulting in Figure 30. Here the user can select the detected range bin from the list on the right and go back to the Virtual Instrument to analyze the selected range bin.

4.2.6 Demo

- The usage of core functions L_statistics, MD_iradon and MD_irdonMC is demonstrated with demo program as presented in Figure 31.

4.3 Time-Frequency Toolbox

The time-frequency analysis toolbox is a set of basic functions used in other toolboxes such as SAR/ISAR toolbox and micro-Doppler toolbox. However, the usage of this toolbox is not limited to the support to other toolboxes. One can use this toolbox in order to get the time-frequency representation of an arbitrary input signal.

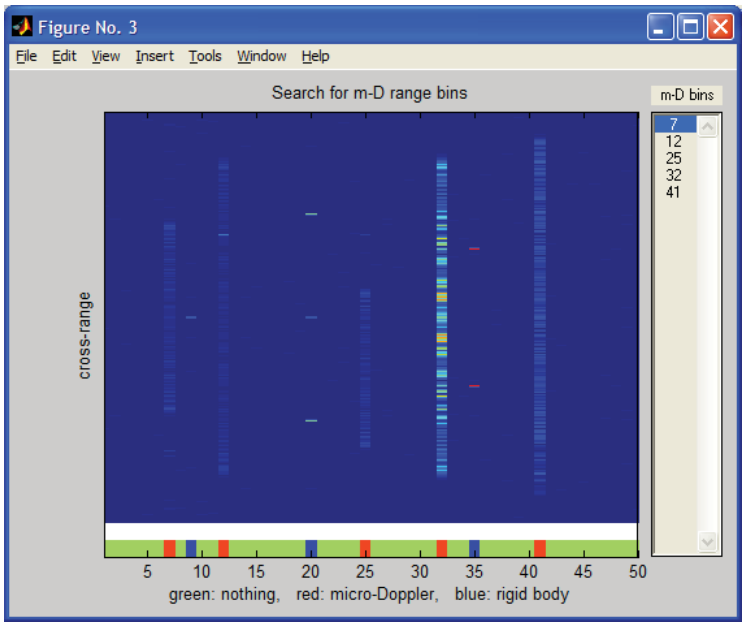

Figure 30: *Range bin selection with 2D input data*

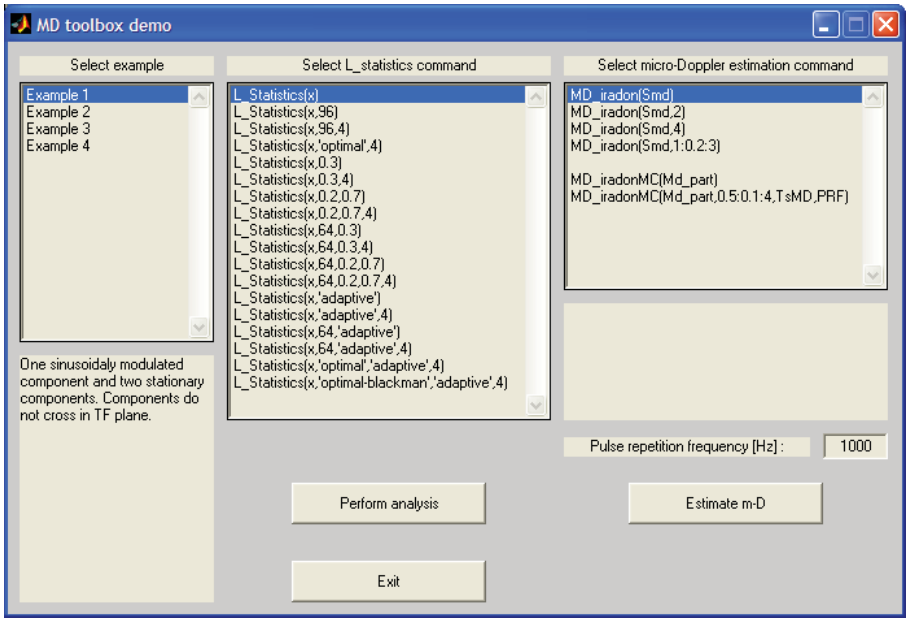

Figure 31: *Range bin selection with 2D input data*

The toolbox provides two time-frequency methods: short-time Fourier transform (STFT) and S-method (SM). A variety of options are added to the core functions, allowing the user, for example, to select the window with constant width or automatically determine the window width in STFT method and use constant L or adaptive S-method. Most of the options are demonstrated by example signals with file `TFR_demo.m`.

4.3.1 Files and installation

The toolbox has four program files:

STFT_TFR.m

SM_TFR.m

ShowData.m

TFR_demo.m

To install the toolbox, copy all the files in the working directory.

4.3.2 Demo

The main toolbox window is presented in Figure 32. The user can select an example signal by using the list on the left. Thereafter the appropriate STFT command should be chosen and finally the S-method command should be selected on the right part.

The user can now click for STFT or S-method calculation and obtain the results as presented in Figure 33 for STFT and Figure 34 for S-method.

4.3.3 Advanced visualization

The advanced visualization options are invoked by typing `ShowData(SM)` at the MATLAB command line for S-method or `ShowData(ST)` for STFT. The result is presented in Figure 35.

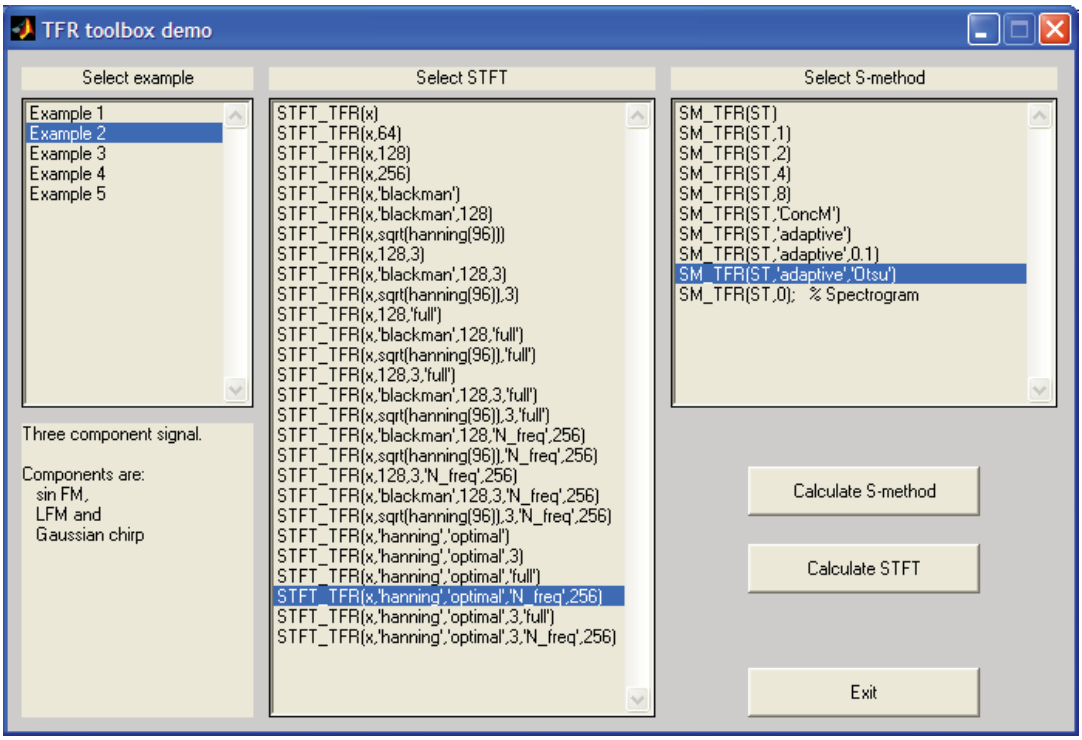

Figure 32: *Time-frequency analysis toolbox demo.*

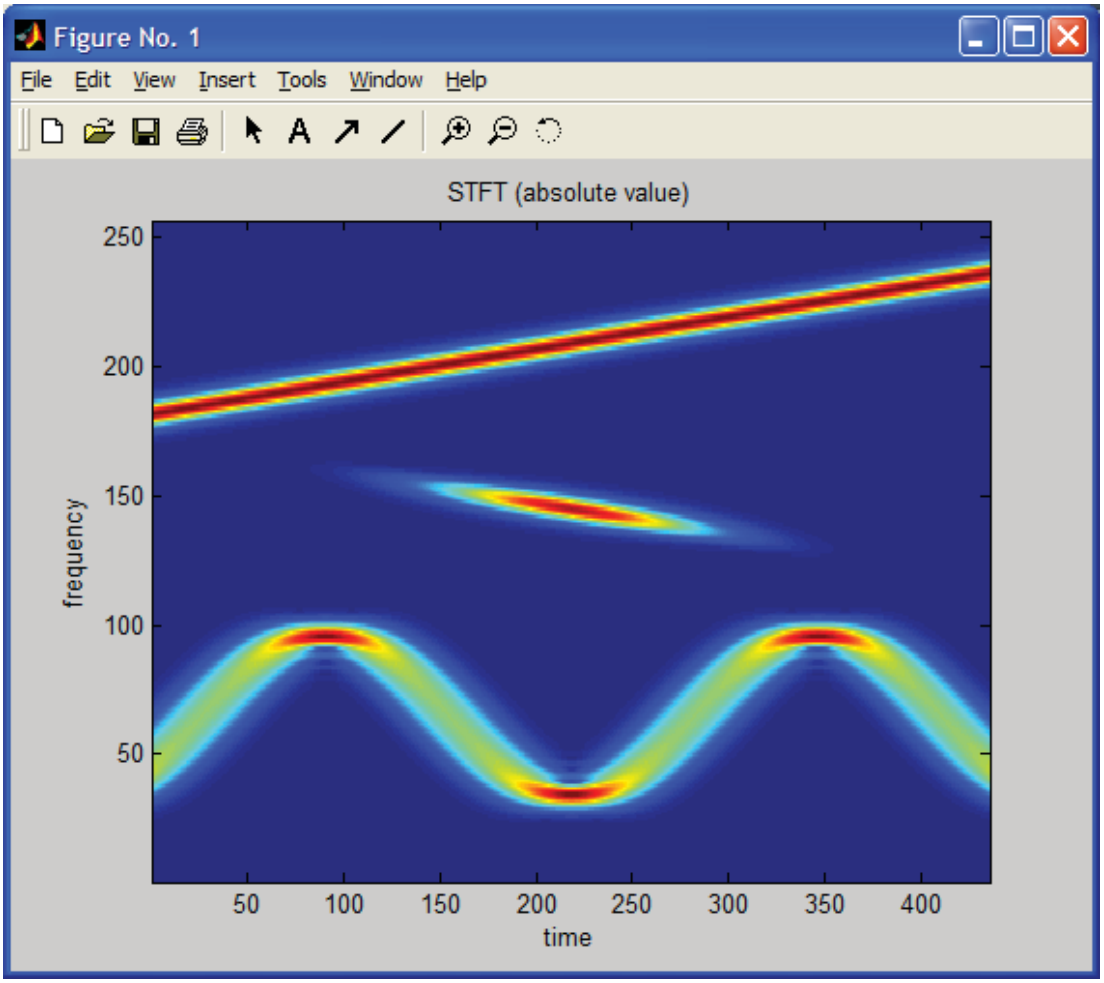

Figure 33: *Short-Time Fourier Transform of the analyzed signal.*

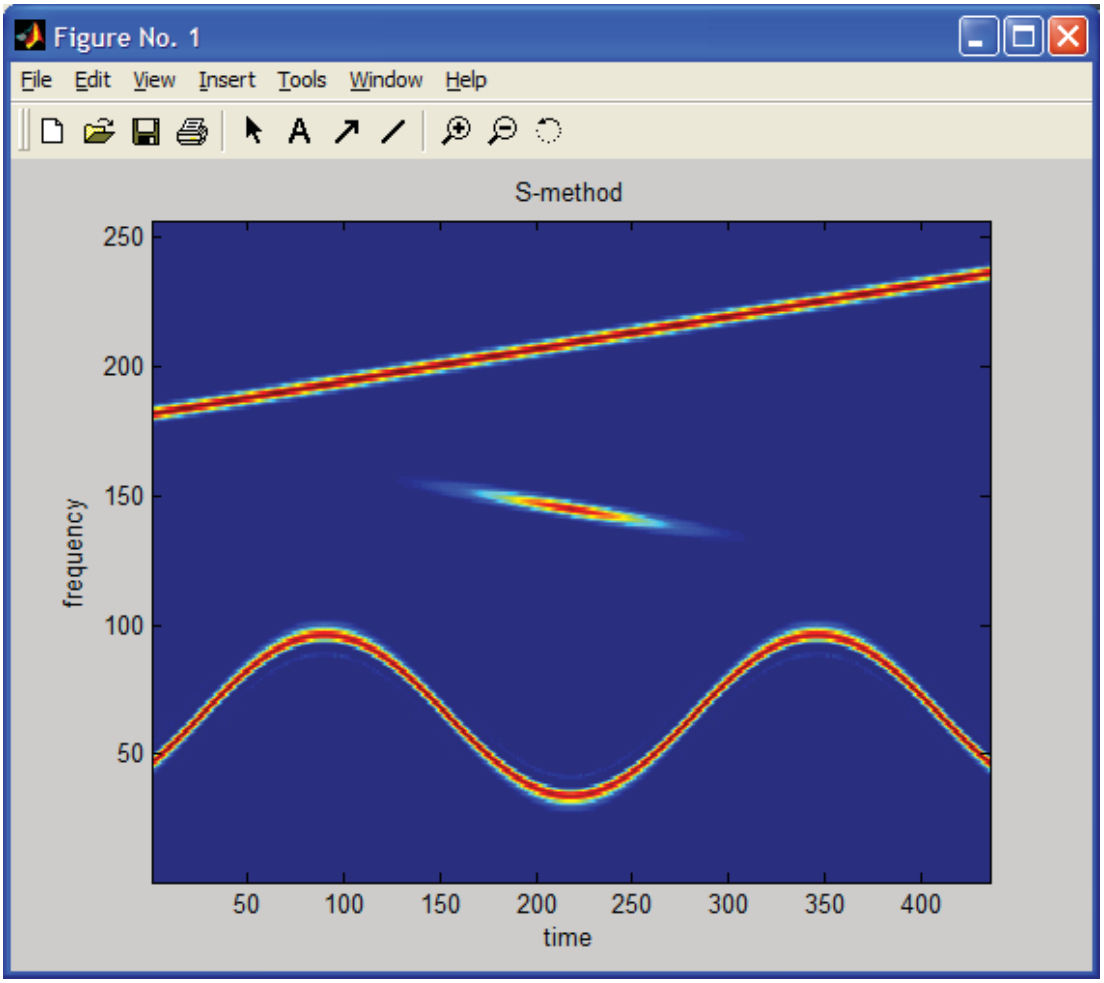

Figure 34: *S-method of the analyzed signal.*

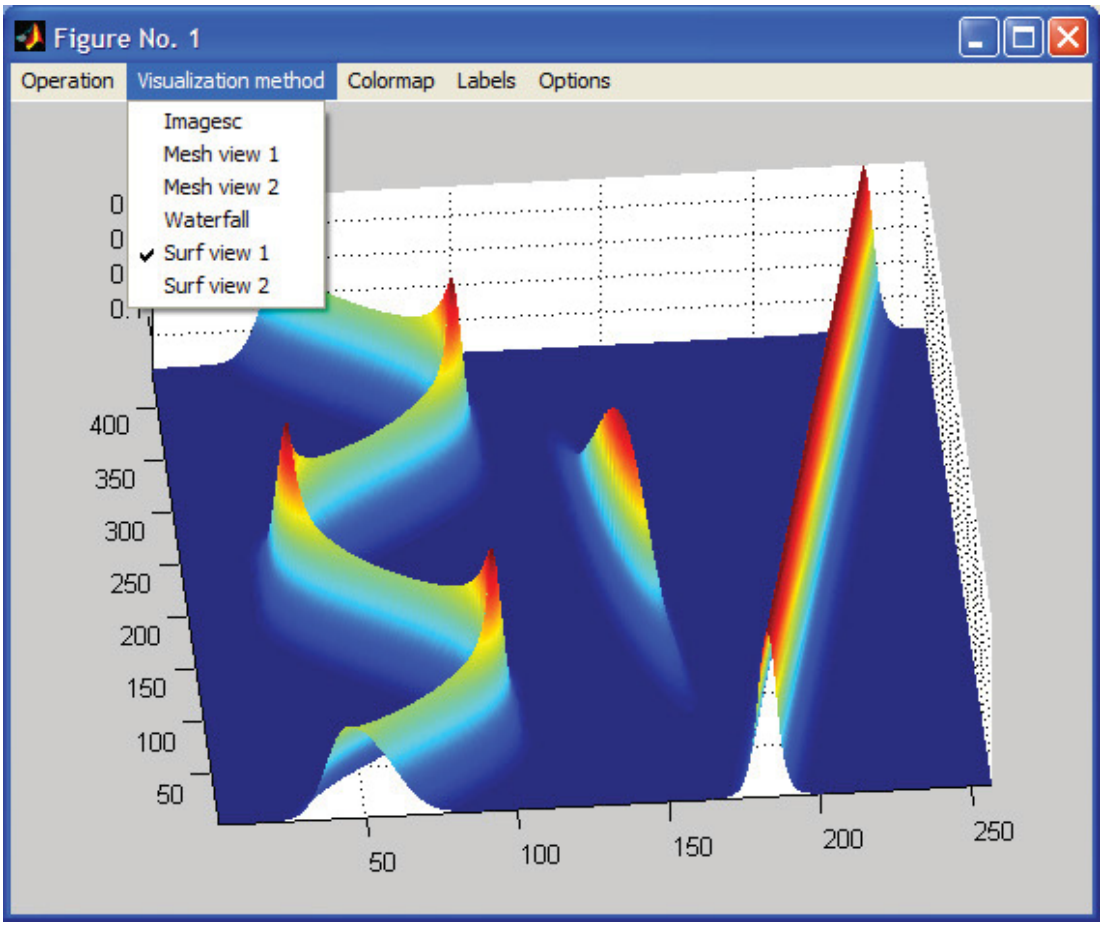

Figure 35: *Advanced visualization options.*

5 Conclusion

A method for estimation of the parameters of sinusoidally modulated signal is introduced. The proposed method is based on the inverse Radon transform and the concentration measures. It is shown that proposed method provides promising estimation and decomposition results for monocomponent and multicomponent signals. The noise and interferences influence upon the estimation procedure is considered. It can be concluded that the proposed method is very robust to the noise and other interferences. We have also shown that the results obtained by the proposed method are meaningful even in cases when the analyzed signal is periodic but not sinusoidally modulated. It can be used to estimate the parameters of periodic extension of a non-periodic time-frequency patterns and partially available data as well.

The m-D effect appears in the ISAR/SAR images in the case when there are fast moving reflectors in the observed scene. The m-D can severely decrease the quality and readability of the obtained radar image. Its detection and removal are very important for obtaining a focused image of the rigid body. In the report, an algorithm for the m-D removal and reconstruction of the rigid body image are proposed. It is based on the L-statistics. Although the L-statistics are already applied by the authors for a similar purpose, the algorithm proposed here is simpler and produces better results. The reconstruction is performed by using only one complex STFT, rather than using several STFTs (with absolute values) and order statistics combination, as it was done in the previous work. Since the proposed algorithm is based on the L-statistics, being a tool for robust signal analysis, it is robust to the effects of noise. Also, it can behave as a high-resolution algorithm, since it can separate close rigid body points. In order to improve the computational efficiency, an adaptive threshold is used to distinguish among STFT samples that correspond to the rigid body and moving parts. Moreover, two additional thresholds are incorporated in the algorithm. The first threshold detects whether there is a returned radar signal in a range bin, while the second threshold detects whether there exist m-D effects in a range bin. Consequently, the procedure for the m-D extraction could be performed only for the range bins where the m-D effect is detected; that could lead to the overall computational savings. Through the examples, it is shown that the proposed algorithm successfully separates the rigid body and the m-D effects.

Based on L-statistics, spectrogram, and inverse Radon transform, a radar data exploitation Matlab toolbox was developed for classifying air and land targets. This toolbox will scan and search any M-D activity in the desired area of the SAR/ISAR image. The toolbox will have three options; 1) Focus the stationary target if there is no M-D, 2) Focus the target after removing the M-D, and 3) extract the M-D and determine the motion parameters such as rotation/vibration rate, initial phase, and amplitude of the stationary and moving targets. The toolbox was tested and validated against a variety of simulated and measured targets.

References

[1] Thayaparan, T., Abrol, S., Riseborough, E., Stanković, L., Lamothe, D., and Duff, G. (2007). Analysis of radar micro-Doppler signatures from experimental helicopter and human data, *IET Proceedings Radar Sonar Navig.*, Vol. 1, No. 4, pp. 288-299.

[2] Thayaparan, T., Suresh, P., and Qian, S. (2010). Micro-Doppler Analysis of Rotating Target in SAR, IET Signal Processing, *IET Signal Processing*, Vol. 4, No. 3, pp. 245-255.

[3] Thayaparan, T., Stanković, L., Daković, M., and Popović, V. (2010), Micro-Doppler parameter estimation from a fraction of the period, *IET Signal Processing*, Vol. 4, No. 3, pp. 201-212.

[4] Thayaparan, T., Stanković, L., and Djurović, I. (2008). Micro-Doppler Based Target Detection and Feature Extraction in Indoor and Outdoor Environments, *J. of the Franklin Institute*, Vol. 345, No. 6, pp. 700-722.

[5] Stanković, L., Thayaparan, T., and Djurović, I. (2006). Separation of target rigid body and micro-Doppler effects in ISAR imaging, *IEEE Trans. Aerosp. Electron. Syst.,* Vol. 41, No. 4. pp. 1,496-1,506.

[6] Chen, V. C., Li, F., Ho, S.-S., and Wechsler, H. (2006). Analysis of micro-Doppler signatures, *IEE Proc. Radar, Sonar, Navig.*, Vol. 150, No. 4, pp. 271-276.

[7] Chen, V. C. (2006). Micro-Doppler effect in radar: Part I: Phenomenon, physics, mathematics, and simulation study, *IEEE Trans. on Aerosp. Electron. Syst*, Vol. 42, No. 1.

[8] Stanković, L., Daković, M, and Thayaparan, T. (2013). *Time-Frequency Signal Analysis With Applications*, Artech House.

[9] Chen, V. C. and Ling, H. (2002). *Time-frequency transforms for radar imaging and signal analysis*, Artech House, Boston.

[10] Li, J. and Ling, H. (2003). Application of adaptive chirplet representation for ISAR feature extraction from targets with rotating parts, *IEE Proc. Radar, Sonar, Navig.*, Vol. 150, No. 4, pp. 284-291.

[11] Sabry, R., Vachon, P. W., Sandirasegaram, N., Secker, J., Liu, C., Mattar, K. E., Wong, S., and Thayaparan, T. (2013). Space-based Radar Products for Military Operations (U): Project 15EL Final Report (U), DRDC Ottawa Research Centre, TR-2013-125.

[12] Mattar, K.E., Guertin, R., Schlingmeier, D., Thayaparan, T., Lukowski, T.I, Sabry, R., Secker, J., Barrie, G. (2013). Makeshift radar reflector trial for search and rescue scenarios. DRDC Ottawa Research Centre, TM-2013-084.

[13] Mattar, K.E., Barrie, G., English, R.A., Liu, C., Sabry, R., Sandirasegaram, N., Secker, J., Thayaparan, T. And, Wolfe, J. (2011). An assessment of Synthetic Aperture Radar feature extraction applications, Ottawa TM 2011-227, DRDC Ottawa.

[14] Vachon, P.W., Barrie, G., Baziuk, W., English, R., Liu, C., Mattar, K., Sabry, R., Sandirasegaram, N., Schlingmeier, D., Secker, J., Thayaparan, T., Wilcox., C., (2009). Synthetic Aperture Radar exploitation: RDE Groups' perspective, DRDC Ottawa, TR 2009-194.

[15] Thayaparan, T., Stankovic, LJ, and Djorovic, I. (2007). Target Detection and Feature Extraction in Indoor and Outdoor Environments using micro-Doppler analysis, DRDC Ottawa, TM 2008-255.

[16] Thayaparan, T. (2006) Separation of target rigid body and micro-Doppler effects in ISAR/SAR, DRDC Ottawa, TM 2006-187.

[17] Thayaparan, T. and Abrol, S. (2005) Micro-Doppler Analysis of Rotating Target in SAR, DRDC Ottawa TM 2005-204, December 2005.

[18] Thayaparan, T., Abrol, S. and Riseborough, E. (2004). Micro-Doppler radar signatures for intelligent target recognition, DRDC Ottawa TM 2004-170.

[19] P. Suresh, T. Thayaparan, K. Venkataramaniah, Micro-Doppler Analysis of Rotating Targets using the Adaptive S- method, International Radar Symposium India 2011, 30 Nov-4 Dec 2011, Bangalore, India.

[20] Thayaparan, T., Stankovic, L., Darkovic, M., Suresh, P., Venkataramaniah, K., SivaSankaraSai, S., Shankar, S., Sairam, T., Nikhilesh. K. (2010). Parameter estimation from a fraction of the period for a rotating target, International Radar Symposium 2010, June 16-18, Lithuania.

[21] Suresh, P., Thayaparan, T., Venkataramaniah, K., SivaSankaraSai, S., and Sridharan, K. S. (2009). Analysis of micro-Doppler radar signatures in SAR using S-method-based, International Radar Symposium India- 2009, December 8-11, Bangalore, India.

[22] Suresh, P., Thayaparan, T., Venkataramaniah, K., SivaSankaraSai, S., and Sridharan, K. S. (2009). Extracting micro-Doppler radar signatures from experimental helicopter data using adaptive Chirplet-based analysis, International Radar Symposium India- 2009, December 8-11, Bangalore, India.

[23] Thayaparan, T., Dakovic, M., Stankovic, L., and Suresh, P. (2009). Intelligent target recognition using micro-Doppler radar signatures, 2009 SPIE Defense, Security, and Sensing, Proceedings of SPIE Volume 7308.

[24] Thayaparan, T., Stankovic, L., and Dakovic, M. (2007). Micro-Doppler Feature Extraction Using S-method, International Radar Symposium - IRS 2006, 5-7 September, Colonge, Germany, pp. 833-837.

[25] Thayaparan, T., Micro-Doppler Feature Extraction using Time-Frequency Analysis, NATO SET-155, Advancing Sensing Thorough the Wall (STTW) Technologies, October 5-7, 2009

[26] Thayaparan, T. , Sensing and Communications Using Ultra-wideband Random Noise Radar, TTCP MAR AG-10 - Maritime Force Protection, CFMWC, MARLANT, Halifax, Nova Scotia, Canada April 20-24, 2009.

[27] Thayaparan, T. and Abrol, Chen, V. C., Analysis of micro-Doppler radar signatures from experimental helicopter and human data, NATO SET-080 symposium, Oslo, Norway, October 11-13, 2004.

[28] Thayaparan, T., Non-stationary Radar Signal Analysis: Time-Frequency Approach, delivered 3-hour Tutorial, International Radar Symposium India 2011, 30 Nov-4 Dec 2011, Bangalore, India

[29] Barbarossa, S. (1995). Analysis of multicomponent LFM signals by a combined Wigner-Hough transform, *IEEE Trans. on Signal Processing*, Vol. 43, No. 6, pp. 1,511-1,515.

[30] Barbarosa S. and Lemoine, O. (1996). Analysis of nonlinear FM signals by pattern recognition of their time-frequency representation, *IEEE Signal Processing Letters*, Vol. 3, No. 4, pp. 112-115.

[31] Stanković, L., Thayaparan, T., Daković, M., and Popović-Bugarin, V. (2013). Micro-Doppler removal in the radar imaging analysis, *IEEE Trans. on Aerospace and Electronics Systems*, Vol. 49, No. 2, pp. 1,234-1,250.

[32] Stanković, L., Thayaparan, T., and Djurović, I. (2006). Separation of Target Rigid Body and Micro-Doppler Effects in ISAR Imaging, *IEEE Trans. on Aerospace and Electronics Systems*, Vol. 42, No. 7, pp. 1,496-1,506.

[33] Ristic, B. and Boashash, B. (1993). Kernel design for time-frequency signal analysis using the Radon transform, *IEEE Trans. on Signal Processing*, Vol. 41, No. 5, pp. 1,996-2,008.

[34] Stanković, S., Djurović, I., and Pitas, I. (2001). Watermarking in the space /spatial-frequency domain using two-dimensional Radon-Wigner distribution, *IEEE Trans. on Image Processing*, Vol. 10, No. 4, pp. 650-658.

[35] Stanković, L. (2001). A measure of some time-frequency distributions concentration, Signal Processing, Vol. 81, No. 3, pp. 621-631.

[36] Wood, J. C. and Barry, D. T. (1994). Linear signal synthesis using the Radon-Wigner distribution, *IEEE Trans. on Signal Processing*, Vol. 42, No. 8, pp. 2,105-2,111.

[37] Wood, J. C. and Barry, D. T. (1994). Radon transformation of time-frequency distributions for analysis of multicomponent signals, *IEEE Trans. on Signal Processing*, Vol. 42, No. 11, pp. 3,166-3,177.

[38] Herman, G. T. (1980). *Image Reconstruction from Projections: The Fundamentals of Computerized Tomography*, Academic Press, New York.

[39] Sommer, H. and Salerno, J. (1971). Radar target identification system, U.S. Patent 3, pp. 614-779.

[40] Marple, S. L. (2001). Large dynamics range time-frequency signal analysis with application to helicopter Doppler radar data, Sixth International Symposium on Signal Processing and its Applications - ISSPA, 13-16 August, Kuala Lumpur, Malaysia.

[41] Zediker, M. S., Rice, R. R., and Hollister, J. H. (1998). Method for extending range and sensitivity of a fiber optic micro-Doppler system and apparatus, U.S. Patent 6,847,817.

[42] Stanković, L., Daković, M., and Ivanović, V. N. (2001). Performance of spectrogram as IF estimator, *Electronics Letters*, Vol. 37, No. 12, pp. 797-799.

[43] Stanković, L. (2004). Performance Analysis of the Adaptive Algorithm for Bias-to-Variance Trade-off, *IEEE Trans. on Signal Processing*, Vol. 52, No. 5, pp. 1,228-1,234.

[44] Bai, X., Zhou, F., Xing, M., and Bao, Z. (2011). High resolution ISAR imaging of targets with rotating parts, *IEEE Trans. on Aerosp. Electron. Syst*, Vol. 47, No. 4, pp. 2,530-2,543.

[45] Totir, F. and Radoi, E. (2009). Superresolution algorithms for spatial extended scattering centers, *Digital Signal Processing,* Vol. 19, No. 5, pp. 780-792.

[46] Martorella, M. (2008). Novel approach for ISAR image cross-range scaling, *IEEE Trans. Aerosp. Electron. Syst.*, Vol. 44, No. 1, pp. 281–294.

[47] Martorella, M. and Berizzi, F. (2005). Time windowing for highly focused ISAR image reconstruction, *IEEE Trans. Aerosp. Electron. Syst.*, Vol. 41, No. 3, pp. 992–1,007.

[48] Wang, Y. and Jiang, Y.-C. (2011). ISAR imaging of ship target with complex motion based on new approach of parameters estimation for polynomial phase signal, *EURASIP Journal on Advances in Signal Processing*, Volume 2011, Article ID 425203.

[49] Sparr, T. and Krane, B. (2003). Micro-Doppler analysis of vibrating targets in SAR, *IEE Proc. Radar Sonar Navig.*, Vol. 150, No. 4, pp. 277-283.

[50] Lyonnet, B., Ioana, C., and Amin, M. G. (2010). Human gait classification using microDoppler time-frequency signal representations, *Radar Conference 2010 IEEE*, 10-14 May, Washington, DC, pp. 915-919.

[51] Djurović, I., Stanković, L., Bohme, J. F. (2003). Robust L-estimation based forms of signal transforms and time-frequency representations, *IEEE Trans. Signal Processing*, Vol. 51, No. 7, pp. 1,753 - 1,761.

[52] Wang, Y., Ling, H., and Chen, V. C. (1998). ISAR motion compensation via adaptive joint time-frequency techniques, *IEEE Trans. Aerosp. Electron. Syst.*, Vol. 38, No. 2, pp. 670-677.

[53] Katkovnik, V. and Stanković, L. (1998). Instantaneous frequency estimation using the Wigner distribution with varying and data driven window length, *IEEE Trans. Signal Processing*, Vol. 46, No. 9, pp. 2,315-2,325.

[54] Yin, P.-Y. (1999). A new circle/ellipse detector using genetic algorithms, *Pattern Recognition Letters*, Vol. 20, No. 7, pp. 731-740.

[55] Misiurewicz, J., Kulpa, K., and Czekala, Z. (1998). Analysis of recorded helicopter echo, Radar 97, 14-16 Oct, Edinburgh, UK., pp. 449-453.

[56] Marple, S. L., (2004). Special time-frequency analysis of helicopter Doppler radar data, in *Time-Frequency Signal Analysis and Processing*, ed. B. Boashash, Elsevier.

[57] Djurović, I., Thayaparan, T., and Stanković, L. (2006). Adaptive local polynomial Fourier transform in ISAR, *EURASIP* Journal of Applied Signal Processing, Vol. 2006, Article ID 36093.

[58] Stanković, L. (2001). A measure of some time–frequency distributions concentration, Signal Processing, Vol. 81, No. 3, pp. 621-631.

This page intentionall left blank.

DOCUMENT CONTROL DATA

(Security markings for the title, abstract and indexing annotation must be entered when the document is Classified or Designated.)

1. ORIGINATOR (The name and address of the organization preparing the document. Organizations for whom the document was prepared, e.g. Centre sponsoring a contractor's report, or tasking agency, are entered in section 8.)

DRDC – Ottawa Research Centre
3701 Carling Avenue, Ottawa ON K1A 0Z4, Canada

2a. SECURITY MARKING (Overall security marking of the document, including supplemental markings if applicable.)

UNCLASSIFIED

2b. CONTROLLED GOODS

(NON-CONTROLLED GOODS)
DMC A
REVIEW: GCEC APRIL 2011

3. TITLE (The complete document title as indicated on the title page. Its classification should be indicated by the appropriate abbreviation (S, C or U) in parentheses after the title.)

A Virtual Instrument for Micro-Doppler Analysis of Signals in SAR/ISAR: Parameters Estimation and Focusing Moving Targets

4. AUTHORS (Last name, followed by initials – ranks, titles, etc. not to be used.)

Thayaparan, T.

5. DATE OF PUBLICATION (Month and year of publication of document.)

April 2014

6a. NO. OF PAGES (Total containing information. Include Annexes, Appendices, etc.)

80

6b. NO. OF REFS (Total cited in document.)

58

7. DESCRIPTIVE NOTES (The category of the document, e.g. technical report, technical note or memorandum. If appropriate, enter the type of report, e.g. interim, progress, summary, annual or final. Give the inclusive dates when a specific reporting period is covered.)

Scientific Report

8. SPONSORING ACTIVITY (The name of the department project office or laboratory sponsoring the research and development – include address.)

DRDC – Ottawa Research Centre
3701 Carling Avenue, Ottawa ON K1A 0Z4, Canada

9a. PROJECT OR GRANT NO. (If appropriate, the applicable research and development project or grant number under which the document was written. Please specify whether project or grant.)

15dp

9b. CONTRACT NO. (If appropriate, the applicable number under which the document was written.)

10a. ORIGINATOR'S DOCUMENT NUMBER (The official document number by which the document is identified by the originating activity. This number must be unique to this document.)

DRDC-RDDC-2014-R6

10b. OTHER DOCUMENT NO(s). (Any other numbers which may be assigned this document either by the originator or by the sponsor.)

11. DOCUMENT AVAILABILITY (Any limitations on further dissemination of the document, other than those imposed by security classification.)

(X) Unlimited distribution
( ) Defence departments and defence contractors; further distribution only as approved
( ) Defence departments and Canadian defence contractors; further distribution only as approved
( ) Government departments and agencies; further distribution only as approved
( ) Defence departments; further distribution only as approved
( ) Other (please specify):

12. DOCUMENT ANNOUNCEMENT (Any limitation to the bibliographic announcement of this document. This will normally correspond to the Document Availability (11). However, where further distribution (beyond the audience specified in (11)) is possible, a wider announcement audience may be selected.) UNLIMITED

13. ABSTRACT (A brief and factual summary of the document. It may also appear elsewhere in the body of the document itself. It is highly desirable that the abstract of classified documents be unclassified. Each paragraph of the abstract shall begin with an indication of the security classification of the information in the paragraph (unless the document itself is unclassified) represented as (S), (C), or (U). It is not necessary to include here abstracts in both official languages unless the text is bilingual.)

The micro-Doppler (m-D) effect appears in the synthetic aperture radar (SAR)/inverse SAR (ISAR) image of a target whenever the target has one or more rotating or vibrating parts. M-D effect introduces distortion in the SAR/ISAR images. On the other hand, m-D effect also carries information about the features of moving parts of a stationary or moving target that can be used for target identification purpose. Based on L-statistics, spectrogram, and inverse Radon transform, a radar data exploitation Matlab toolbox was develped for classifying air, land and ocean targets, which helps Geospatial Intelligence (GEOINT) support to Canadian Forces. This toolbox will scan and search any M-D activity in the desired area of the SAR/ISAR image. The toolbox has three options; 1) Focus the stationary target if there is no m-D, 2) Focus the target after removing the m-D, and 3) extract the m-D and determine the motion parameters. The toolbox was tested and validated against a variety of simulated and measured targets.

14. KEYWORDS, DESCRIPTORS or IDENTIFIERS (Technically meaningful terms or short phrases that characterize a document and could be helpful in cataloguing the document. They should be selected so that no security classification is required. Identifiers, such as equipment model designation, trade name, military project code name, geographic location may also be included. If possible keywords should be selected from a published thesaurus. e.g. Thesaurus of Engineering and Scientific Terms (TEST) and that thesaurus identified. If it is not possible to select indexing terms which are Unclassified, the classification of each should be indicated as with the title.)

Micro-Doppler; Fourier Transform; Time-Frequency Analysis; Short-Time Fourier Transform; Radon Transform; L-Statistics; Geospatial Intelligence; Radar Detection; Classification; SAR; ISAR

DRDC | RDDC

SCIENCE, TECHNOLOGY AND KNOWLEDGE
FOR CANADA'S DEFENCE AND SECURITY

SCIENCE, TECHNOLOGIE ET SAVOIR
POUR LA DÉFENSE ET LA SÉCURITÉ DU CANADA

www.drdc-rddc.gc.ca